Published in Chemical Geology 25, issues 1-2, 143-159, 2008
which should be used for any reference to this work

Emplacement of ultramafic rocks into the continental crust monitored by light and other trace elements: An example from the Geisspfad body (Swiss-Italian Alps)

Laure Pelletier [a,*], Othmar Müntener [b], Angelika Kalt [a], Torsten W. Vennemann [b], Tamás Belgya [c]

[a] Institute of Geology and Hydrogeology, University of Neuchâtel, Emile Argand 11, CP158, 2009 Neuchâtel, Switzerland
[b] Institute of Mineralogy and Geochemistry, University of Lausanne, Anthropole, 1015 Lausanne, Switzerland
[c] Institute of Isotopes, Hungarian Academy of Sciences, P.O. Box 77, 1525 Budapest, Hungary

Editor: R.L. Rudnick

A B S T R A C T

In order to evaluate the influence of continental crustal rocks on trace element budgets of serpentinized peridotites incorporated into the continental crust, we have analyzed the chemical composition of whole rock samples and minerals of the Geisspfad ultramafic complex (Swiss-Italian Alps). This complex represents a relict oceanic succession composed of serpentinites, ophicarbonates and metabasic rocks, emplaced into crustal gneisses during Alpine collision. Following peak metamorphic amphibolite facies conditions, fluid flow modified some of the trace element contents of ophicarbonates and deformed serpentinites close to the contact with country rocks. The fluid originated from the surrounding continental crustal rocks as documented by the increase of Pb in the serpentinites, and by the strongly negative ∂D values (−112‰) of some ultramafic rocks close to the contact with surrounding gneisses. Little or no modification of the fluid mobile elements Li, B or U was observed in the serpentinite. In-situ analysis of light elements of serpentinite minerals indicate redistribution of light elements coupled to changes of mineral modes towards the outer 100–150 m of the massif. In the centre of the massif, Li is preferentially concentrated in olivine, while Be and B are hosted by tremolite. In contrast, at the outer rim of the massif, Li and Be are preferentially incorporated into diopside, and B into antigorite. This redistribution of light elements among the different minerals is visible in the serpentinite, at a maximum distance of ~100–150 m from the ophicarbonate–metabasite contact. Our results show that interaction of ultramafic rocks and crust-derived fluids can be easily detected by studies of Pb and ∂D in whole rocks. We argue that small ultramafic bodies potentially record an emplacement-related trace element signature, and that crustal light element values in ultramafic rocks are not necessarily derived from a subducting slab.

Keywords: Lithium Beryllium Boron Serpentinite Fluid flow

1. Introduction

In the last decade, Li and B have proven to be powerful tracers of fluid-related metasomatic processes, in addition to more 'conventional' large ion lithophile elements (Seyfried et al., 1984; You et al., 1995; Leeman, 1996; Brenan et al., 1998b), because they are extremely fluid mobile under a wide range of temperature, and because their stable isotopes (^{6}Li, ^{7}Li, ^{10}B, ^{11}B) can fractionate during these processes (Spivack and Edmond, 1987; Palmer, 1991; Chan et al., 1992; Noll et al., 1996; Palmer, 1996; Benton et al., 2001, 2004; Decitre et al., 2002; Rosner et al., 2003; Tomascak, 2004; Teng et al., 2006). Li and B have been studied for some years in serpentinites from mid-ocean ridges (Bonatti et al., 1984; Früh-Green et al., 1996; Decitre et al., 2002; Niu, 2004; Paulick et al., 2006), forearc (Benton et al., 2001, 2004; Savov et al., 2005, 2007; Wei et al., 2005), and ophiolitic environments (Scambelluri et al., 2004; Pelletier et al., in review), as well as in rare high pressure serpentinites (Scambelluri et al., 2004; Marschall, 2005). These studies demonstrate that the interaction between peridotite and seawater may lead to a considerable enrichment of serpentinites in B, and to a lesser extent in Li. In the Mariana forearc serpentinites, Li enrichment is more pronounced than at mid-ocean ridges, and is related to slab-derived fluids released by the subducting oceanic lithosphere (Benton et al., 2004). The Beryllium content of drilled mid-ocean ridge and ophiolitic serpentinites is extremely low (e.g., ODP Leg 209: Vils et al. (accepted), Pindos ophiolite: Pelletier et al., (in review)), while the Be content of dredged mid-ocean ridge serpentinites is low but highly variable (Niu, 2004). These data provide information about the potential input of light elements into subduction zones via serpentinites.

Recently, Scambelluri et al. (2004) studied the Li and B composition of the oceanic mantle under increasing pressure and temperature during Alpine subduction, using samples from the Alps, the Northern Apennine and the Sierra Nevada in Southern Spain. They showed that there is a progressive release of oceanic B with increasing pressure and temperature into the metamorphic fluid, but also that a significant quantity of B can be retained in high pressure phases (olivine and Ti-clinohumite),

* Corresponding author. Tel.: +41 32 718 26 80; fax: +41 32 718 26 01.
E-mail addresses: laure.pelletier@unine.ch (L. Pelletier), othmar.muntener@unil.ch (O. Müntener), angelika.kalt@unine.ch (A. Kalt), torsten.vennemann@unil.ch (T.W. Vennemann), belgya@alpha0.iki.kfki.hu (T. Belgya).

and potentially transported to the deep mantle. Scambelluri et al. (2004) showed that the Li content of high pressure peridotites (4.9 μg/g; Betic Cordillera) derived from an oceanic serpentinite precursor might exceed those of oceanic serpentinites (1.3 μg/g; Erro Tobbio unit), suggesting a potential input from an external source. Marschall (2005) studied Li, Be and B contents in high pressure serpentine and serpentinites of northern Syros (Greece) and Pfulwe Pass (Switzerland). The Syros serpentinites have Li (0.9–2.8 μg/g) and B (5.5–11.3 μg/g) concentrations lower than those of the altered oceanic mantle (Li: ~3.5 μg/g, Decitre et al., 2002; B: 20–100 μg/g, Thompson and Melson, 1970; Bonatti et al., 1984; Spivack and Edmond, 1987), but are clearly enriched in Be (0.2–0.5 μg/g) compared to these rocks (~0.04 μg/g; Niu, 2004).

In order to study the slab-to-mantle wedge transfer trace element contents of high pressure garnet peridotites were investigated (Paquin et al., 2004; Scambelluri et al., 2006). Both data sets suggest a metasomatic overprint of mantle rocks by subduction-related fluid or melt, which modified the trace and light element budget of the peridotites. In the Alpe Arami peridotites, addition of Li, a limited addition of B and no change in the Be contents were determined (Paquin et al., 2004). In the Ulten peridotites, addition of Li, and to a lesser extent in Be were measured (Scambelluri et al., 2006).

All these studies focused on subducted serpentinites and high pressure wedge peridotites, but they did not discuss the potential light element transfer during incorporation of these rocks into the crust. Li and Be contents of the continental crust (Rudnick and Gao, 2004 and references therein) are much higher than those of serpentinites or unmetasomatized peridotites (e.g., Decitre et al., 2002; e.g., review by Niu, 2004; Ottolini et al., 2004). The boron content of the continental crust (Rudnick and Gao, 2004 and references therein) is lower than, or comparable to that of serpentinites (Spivack and Edmond, 1987 and references therein), but clearly higher than values for unmetasomatized mantle. The modification of (light) element budgets of ultramafic bodies during emplacement into the continental crust is poorly constrained, and it remains to be tested whether the light element systematics observed in high pressure mantle rocks are exclusively related to subduction zone processes. Trace element data on ultramafic bodies that were not subducted, but incorporated into the continental crust are thus needed for improved estimates of subduction-related imprints. The Geisspfad ultramafic massif meets these criteria.

The objective of this study is to characterize the chemical composition, (both minerals and whole rocks) of serpentinized peridotites during regional metamorphism in a continental environment. Samples of ultramafic rocks were collected along several profiles through the Geisspfad massif, to determine possible variations of trace element contents and to determine the Li, Be and B contents of minerals and whole rocks. In addition we determined $\delta^{18}O$ and δD for selected samples. These data collectively suggest that crustal trace element signatures in ultramafic rocks cannot be uniquely assigned to subduction-related processes.

2. Geological setting

The Geisspfad ultramafic massif (Valais, Switzerland) is one of the largest ultramafic bodies in the Central Alps (Pastorelli et al., 1995) and is incorporated into the lower Penninic Monte Leone nappe (Fig. 1; Keusen, 1972; Pastorelli et al., 1995), which includes crystalline basement rocks and an overturned Mesozoic sedimentary cover. The nappe belonged to the distal European margin before the Alpine collision. In the Geisspfad region, the Monte Leone nappe includes gneisses of magmatic and sedimentary origin, Triassic dolomitic marbles and some calcschists (Pastorelli et al., 1995). The Geisspfad body and the gneiss were both metamorphosed under amphibolite facies conditions (Keusen, 1972) during Alpine metamorphism, meaning that the Geisspfad massif was certainly incorporated into the gneiss prior to this metamorphic event. Age and paleogeographic position of the Geisspfad ultramafic body are largely unknown.

Pastorelli et al. (1995) estimated temperatures between 520 and 560 °C and pressures between 0.6 and 0.7 GPa for this metamorphism, selecting plagioclase-hornblende pairs in metabasites and using the geothermobarometer of Plyusnina (1982).

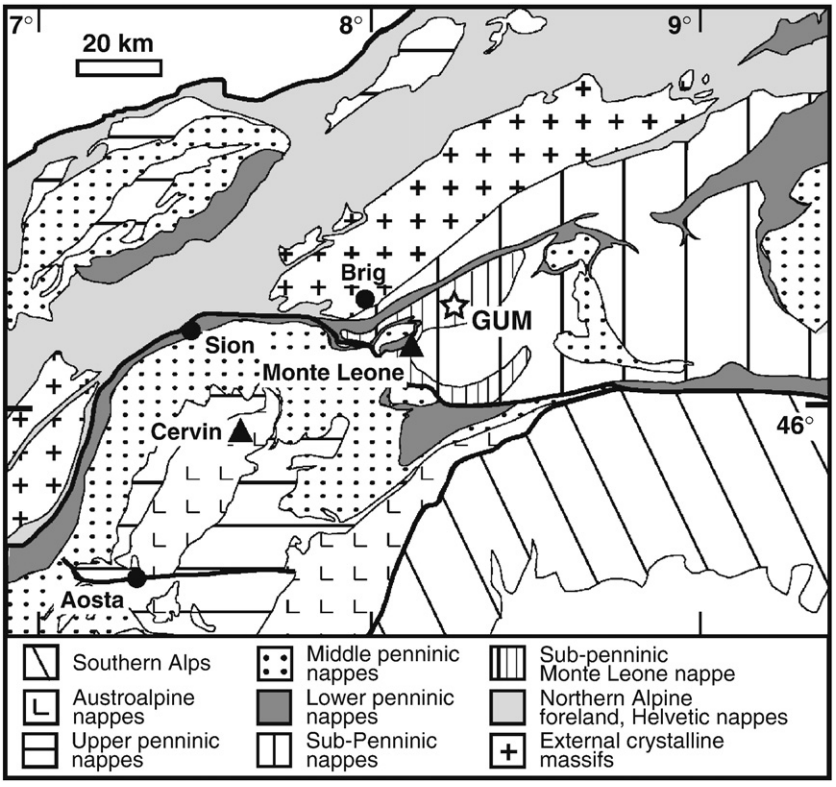

Fig. 1. General tectonic overview of the Central Alps (modified after Schmid et al., 2004). GUM: Location of the Geisspfad ultramafic massif.

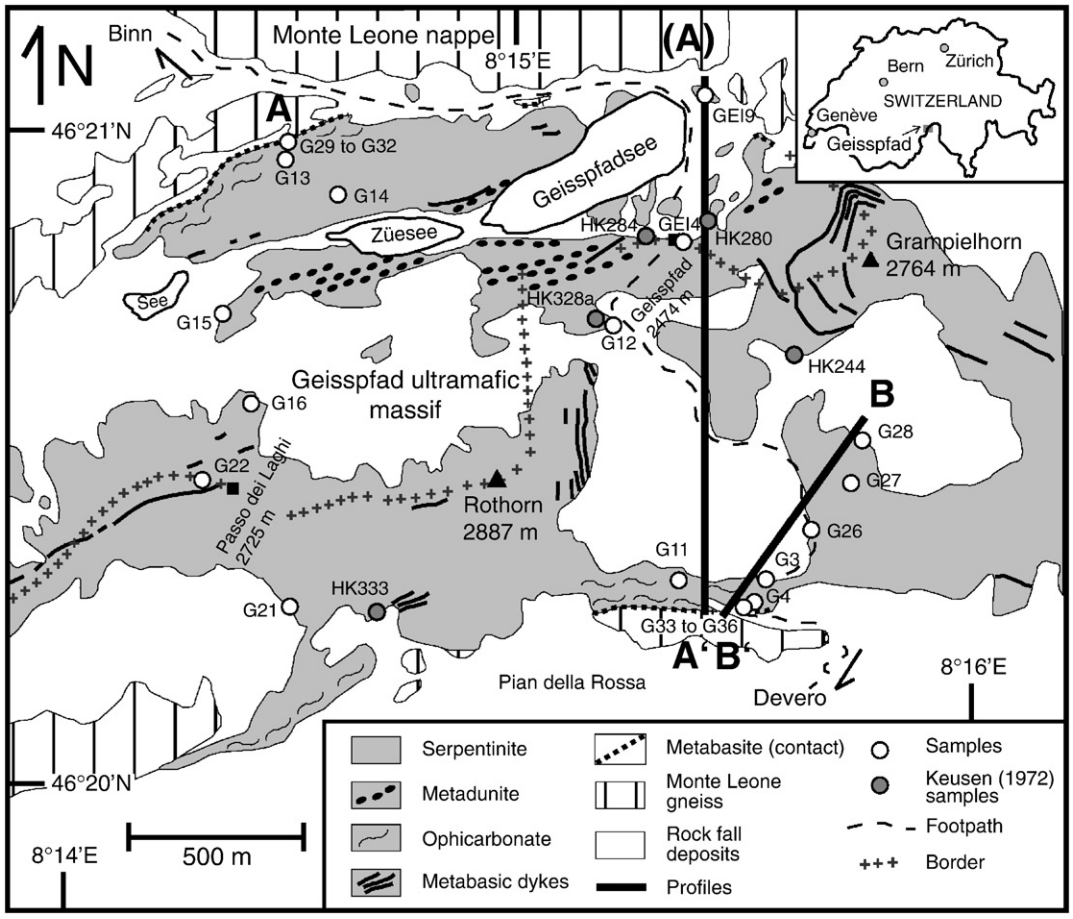

Fig. 2. Simplified geological map of the Geisspfad ultramafic massif (modified after Keusen, 1972), illustrating the contact between the ultramafic unit and the surrounding Monte Leone nappe. Profiles A–A′ and B–B′ refer to Fig. 3.

The Geisspfad ultramafic body is composed of various ultramafic and mafic rocks, mainly serpentinite, ophicarbonate and metabasic dykes (Fig. 2; Keusen, 1972; Pastorelli et al., 1995). Keusen (1972) and Pastorelli et al. (1995) defined a lherzolitic origin for the mantle protolith. In a fresh granular lherzolite from the Geisspfad ultramafic body, Pastorelli et al. (1995) described assemblages of orthopyroxene +

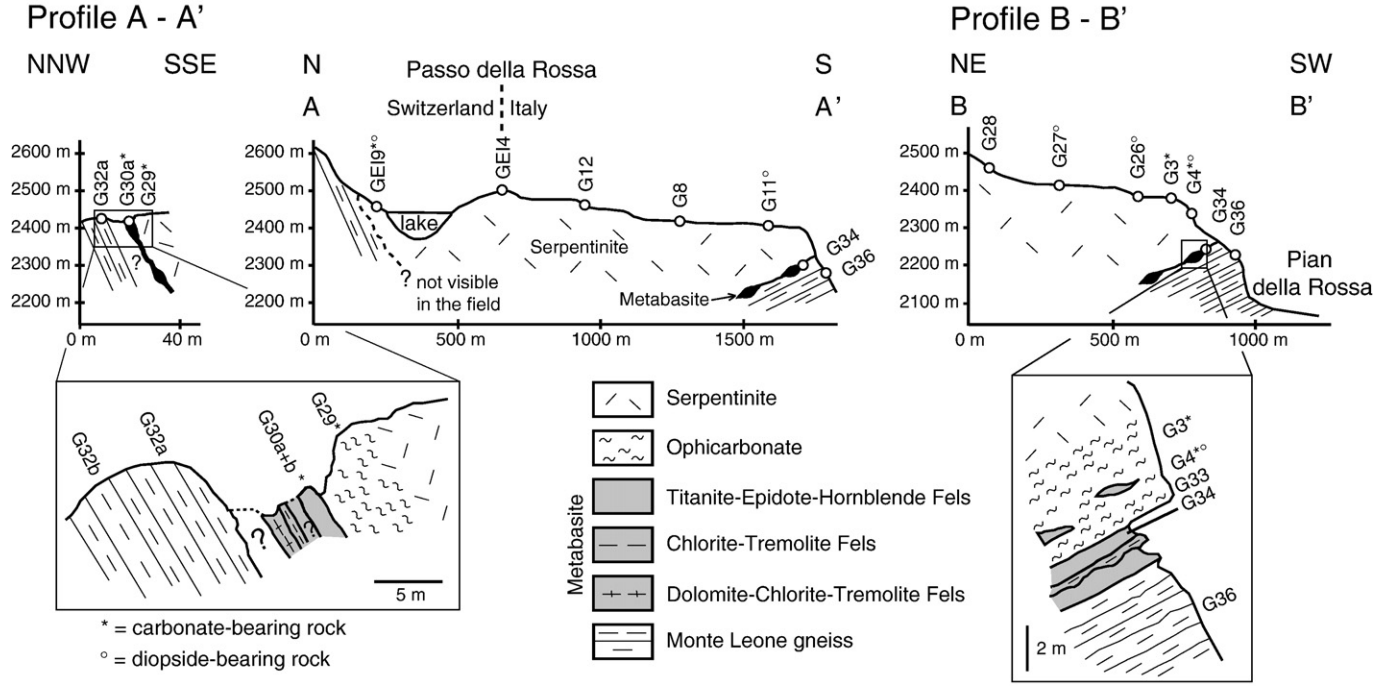

Fig. 3. Profiles of the contact between the ultramafic unit and the gneiss of the Monte Leone nappe, with position of the studied samples.

clinopyroxene + spinel, which might represent breakdown products of precursor garnet. However, this fresh lherzolite was collected in loose blocks (east of Rothorn, Pastorelli S. personal communication), and was not found during sampling for the present study. The inferred garnet to spinel facies transition could be related to uplift from deep lithospheric levels towards the sea floor. Metabasic dykes show a MORB tholeiitic affinity, and are usually rodingitized (Pastorelli, 1994). Pastorelli et al. (1995) concluded that the Geisspfad ultramafic body represents a piece of exhumed subcontinental mantle, which was probably emplaced in an ocean–continent transition environment during pre-Alpine rifting, by analogy to other ultramafic bodies in the Alps and Apennine (e.g., Müntener et al., 2000; Manatschal et al., 2003).

Different mafic lithologies were found at the contact between the Monte Leone gneiss and the serpentinite (Keusen, 1972) and were interpreted as metabasalt and metagabbros (Pastorelli et al., 1995) (Figs. 2–3). They show a MORB affinity similar to metabasic dykes from the inner part of the massif, and they are generally rodingitized. Keusen (1972) mentioned the presence of ophidolomite in contact with the serpentinite.

3. Analytical techniques

About 500 g of each sample were powdered in a tungsten mill. Before milling, rocks were cut with a rock saw, in order to obtain clean blocks and to remove weathering. Rock powders were checked optically, in order to confirm that all minerals were powdered.

Major element contents of whole rock samples were measured by wavelength dispersive X-ray fluorescence (WD-XRF) at the Geosciences

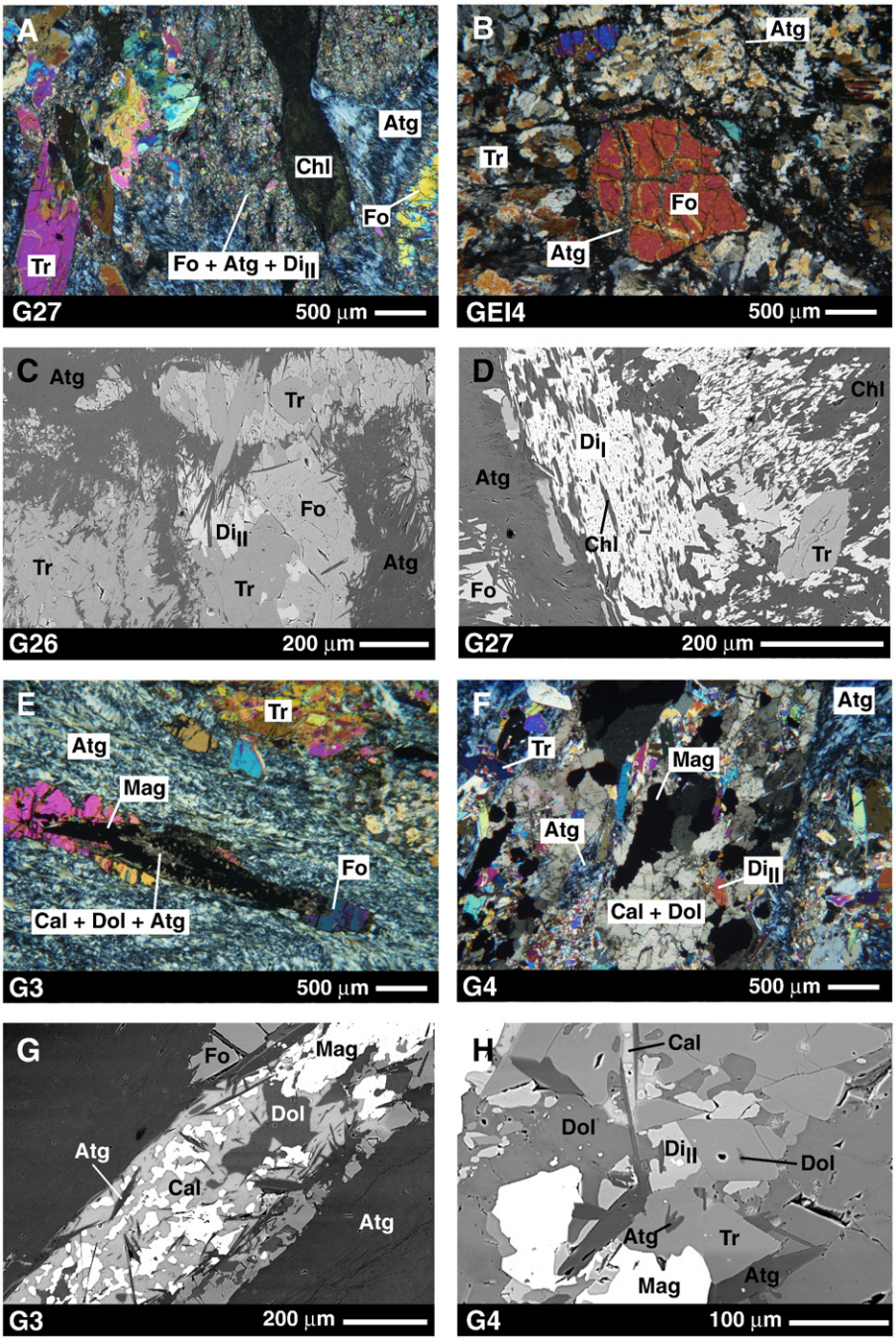

Fig. 4. Texture and mineralogy of the studied serpentinites (A to D) and ophicarbonates (E to H). A, B, E, F: photomicrographs taken in cross-polarized light. C, D, G, H: backscattered electron images. Abbreviations: Atg: antigorite, Cal: calcite, Chl: chlorite, Di_I: primary diopside, Di_{II}: secondary diopside, Dol: dolomite, Fo: forsterite, Ilm: ilmenite, Mag: magnetite, Tr: tremolite.

Department of the Fribourg University (Switzerland). Two grams of powder of each sample were dried for 6 to 12 h in a furnace (110 °C), and the loss of weight was measured (humidity). Powders were later put in a furnace at 1000 °C for an hour under an oxidizing atmosphere. The final loss of weight was determined (Loss On Ignition, LOI), which represents the total loss of volatiles (H_2O and CO_2) and a gain of weight by oxidation of Fe^{2+}. 0.70 g of this dry powder was mixed with 6.65 g of dried lithium tetraborate ($Li_2B_4O_7$) and 0.35 g of dried lithium fluoride (LiF). This mix was put in a Pt–Au–ZrO crucible, in order to obtain a glass after 10 min heating at 1150 °C with a PHILIPS PERL'X-2. These glasses were measured with a PHILIPS PW1400 X-ray fluorescence spectrometer. Detection limit was ~0.01 wt.% and external reproducibility (1σ) between 0.5 and 5% depending on the element. A correction factor was applied to the analytical results considering the calibration of the instrument with international reference standards (BHVO-1, DNC-1, W-2, JB-3; Govindaraju, 1994). Standard data can be found in Table G in Appendix A.

Li, Be and trace element whole rock contents were measured by inductively coupled plasma mass spectrometry (ICP-MS), using a VG PQ ExCell quadrupole ICP-MS at the Boston University. All the details concerning sample preparation, ICP parameters and standards used are described in Kelley et al. (2003). Standard data related to the present study can be found in Table H in the Appendix A. The protocol given by Kelley et al. (2003) was followed, except for the final sample dilution (1/1000 instead of 1/2000). Element concentrations were measured in analogue mode, for high-abundance elements (>5 ng/g in solution). For elements <5 ng/g in solution (e.g., REE, Rb, Y, Ba, and Zr), a pulse counting mode was applied. DNC-1 (USGS) standard reference material was run as an unknown and also compared with the values of Kelley et al. (2003). Precision was evaluated by the measurement of in-run replicates showing a relative standard deviation (RSD, 1σ) <2–3% for all elements. Precision decreases with decreasing abundance, and RSD (1σ) can reach 5% for low-abundance elements.

B, S, Cl, and H_2O whole rock contents were measured by Prompt Gamma Neutron Activation Analysis (PGNAA) at the facility of the Budapest Research Reactor (BRR). B, S, Cl and H_2O whole rock contents in geological samples were determined previously with high precision by this method (Gméling et al., 2005; Marschall et al., 2005; Pelletier et al., in review). All details concerning analytical procedure can be found in Molnár (2004), Révay et al. (2004), Szakmány and Kasztovszky (2004) and Marschall et al. (2005). PGNAA is particularly useful for analyzing whole rock boron concentrations, because no sample preparation is needed, which avoids contamination problems (Anderson and Kasztovszky, 2004). The principle of the PGNAA method is the detection of prompt γ-rays that originate from the (n,γ)-reactions during neutron irradiation (Révay and Belgya, 2004). The detection limit for boron (0.01 to 0.03 μg/g) was different in each sample, depending on measurement time and sample weight. Relative uncertainty (1σ) is small (1 to 2%), and can reach 5% if the B content is lower than 1 μg/g. Relative uncertainties for S, Cl and H_2O were calculated at 6 to 8, 6 to 18 and 2 to 3%, respectively. Detection limits were approximately 500 μg/g for S, 28 μg/g for Cl and 10 μg/g for H_2O. All details concerning the standards used can be found in Gméling et al. (2005).

The oxygen isotope composition (^{16}O, ^{17}O, ^{18}O) of the samples was measured at the University of Lausanne (Switzerland), using a method similar to that described by Sharp (1990) and Rumble and Hoering (1994), and described in more detail by Kasemann et al. (2001). Between 0.5 to 2.0 mg of sample rock powder were loaded into a small Pt-sample holder and pumped out to a vacuum of about 10^{-6} mbar. After prefluorination of the sample chamber overnight, the samples were heated with a CO_2 laser in pure F_2 at 50 mbars of pressure. Excess F_2 was separated from O_2 produced by conversion to Cl_2 using KCl held at 150 °C. The extracted O_2 was collected on a molecular sieve (5A) and subsequently expanded into the inlet of a Finnigan MAT 253 mass spectrometer. Oxygen isotope compositions are given in the standard δ-notation, expressed relative to VSMOW in permil (‰). Replicate oxygen isotope analyses of an in-house standard, LS-1 quartz (N=2), gave a precision of better than 0.1‰ (1s) for $\delta^{18}O$. The accuracy of $\delta^{18}O$ values is commonly better than 0.2‰ (1s) compared to accepted $\delta^{18}O$ values for LS-1 of 18.10‰. Standard data related to the present study can be found in Table I in Appendix A.

Hydrogen isotope compositions of whole rock powders were measured at the University of Lausanne (Switzerland), using high-temperature (1450 °C) reduction methods with He carrier gas and a TC-EA linked to a Delta Plus XL mass spectrometer from Thermo-Finnigan on 2 to 4 mg sized samples according to a method following Sharp et al. (2001). The results are given in the standard δ-notation, expressed relative to VSMOW in permil (‰). The precision of the in-house kaolinite standard and NBS-30 biotite for hydrogen isotope analyses was better than ±2‰ (1σ) for the method used; all values were normalized using a value of −125‰ for the kaolinite standard and −65.7‰ for NBS-30 analyzed during the same period as the samples. Standard data related to the present study can be found in Table I in Appendix A.

Light element compositions of minerals were measured in situ by secondary ion mass spectrometry (SIMS) with a modified Cameca 3f ion microprobe (equipped with a primary beam mass filter) at the Institute of Mineralogy of the Ruprecht-Karls University of Heidelberg (Germany). A protocol minimizing boron surface contamination during sample preparation and measurements was followed (Marschall and Ludwig, 2004). SIMS measurements were performed on points previously measured by electron microprobe. The primary $^{16}O^-$ ion beam was set to 14.5 keV at a current of 20 nA. Positive secondary ions were accelerated to 4.5 keV and the energy window was set to 40 eV. The energy filtering technique was applied with an offset of ~75 eV at a mass resolution m/Δm (10%) of ~1020. Quantitative results were obtained using relative sensitivity factors with ^{30}Si as reference isotope for silicates (Ottolini et al., 1993), and ^{44}Ca for carbonates. Detection limits (the critical value; Currie, 1968) during silicate measurements for samples G3, G4 and G27 were calculated at 2.0, 2.0 and 3.7 ng/g for Li, Be and B, respectively. For the other samples, values were lower at 1.4 for Li, 1.0 for Be and 2.6 ng/g for B. Detection limits for carbonate measurements were calculated at 1.4, 1.0 and 2.6 ng/g for Li, Be and B, respectively. All rock-forming minerals were analyzed, except for oxides and sulphides. For carbonates, SRM610 glass was used as a standard which contains about 2 wt.% CaO, which is much lower than CaO content in carbonates. Moreover, there is probably a matrix effect between silicates and carbonates, which is unknown. The results presented in this paper for carbonates are hence approximate values, and may be off by a factor of two (T. Ludwig, personal communication).

4. Sample description and mineralogy

Two different types of ultramafic rocks are present in the Geisspfad body. They are distinguishable by their degree of deformation and by

Table 1
Modal composition of some serpentinite and ophicarbonate

Rock	Sample	D (m)	Atg (%)	Di (%)	Tr (%)	Fo (%)	Other (%)	
Serp	G12	727	18		18	45	19	Chl, Mag
Serp	GEI4	416	16		21	46	17	Chl, Mag
Serp	G27	310	37	2	5	42	14	Chl, Mag
Serp	G26	174	32	4	4	59	1	Chl, Mag
Serp	G11	115	38	6	6	43	7	Chl, Mag
Ophi	GEI9	59	73	3	10		14	Chl, Mag, Ilm, Cal
Ophi	G3	48	74		4	20	2	Mag, Ilm, Cal, Dol
Ophi	G4	16	88	2	3		7	Mag, Ilm, Cal, Dol

Abbreviations: Atg = antigorite, Di = diopside, Tr = tremolite, Fo = forsterite, Chl = chlorite, Mag = magnetite, Ilm = ilmenite, Cal = calcite, Dol = dolomite, Serp = serpentinite, Ophi = ophicarbonate. D (m) = nearest orthogonal distance to the ophicarbonate–metabasite contact.
Samples presented in this table were analyzed by Secondary Ions Mass Spectrometry (SIMS) for their Li, Be and B content in minerals.

Table 2
Whole rock composition of serpentinite and ophicarbonate

		Rock	Serp	Serp	Serp	Serp	Serp	Serp	Serp	Serp	Serp	Serp	Serp	Serp	Ophi	Ophi	Ophi	Ophi	Ophi
		Sample	GEI4	G11	G12	G14	G15	G16	G21	G22	G26	G27	G28	G29	G3	G4	GEI9	G13	G33
		D (m)	416	115	727	208	328	607	370	636	174	310	511	3	48	16	59	54	1
		Lat N	133113	132126	132856	133236	132901	132643	132088	132441	132283	132421	132531	133371	132133	132098	133536	133376	132098
		Long E	662937	662907	662717	661957	661619	661702	661814	661539	663279	663397	663417	661759	663147	663142	662975	661817	663142
Method	Element	Unit																	
XRF	SiO_2	wt.%	44.21	44.70	45.00	44.84	43.97	44.32	44.86	43.69	43.94	43.67	43.80	46.93	45.69	44.68	45.18	44.87	48.76
	TiO_2	wt.%	0.18	0.09	0.15	0.19	0.06	0.09	0.24	0.18	0.06	0.19	0.14	0.09	0.09	0.17	0.23	0.20	0.08
	Al_2O_3	wt.%	3.13	1.72	2.60	3.14	0.58	1.07	3.42	2.83	0.62	2.58	2.13	1.50	1.40	3.20	3.53	3.14	1.55
	Cr_2O_3	wt.%	0.36	0.42	0.38	0.38	0.55	0.39	0.36	0.35	0.37	0.34	0.34	0.37	0.41	0.35	0.38	0.38	0.34
	Fe_2O_3	wt.%	10.00	8.96	8.39	9.44	8.99	9.05	9.33	10.15	9.51	9.73	10.67	7.50	8.93	8.58	9.53	9.46	9.07
	MnO	wt.%	0.15	0.13	0.12	0.12	0.12	0.14	0.13	0.14	0.14	0.13	0.16	0.12	0.12	0.11	0.13	0.12	0.11
	MgO	wt.%	39.24	41.93	40.80	39.04	45.53	42.21	38.52	40.01	44.06	42.19	40.57	44.01	41.94	40.50	36.36	39.07	35.99
	CaO	wt.%	3.06	2.66	2.62	2.83	0.19	2.92	3.34	2.61	1.68	1.59	2.55	0.02	1.41	2.50	4.70	2.83	4.12
	Mg#		0.89	0.91	0.91	0.90	0.91	0.91	0.89	0.89	0.91	0.90	0.89	0.92	0.91	0.91	0.89	0.90	0.89
	LOI	wt.%	4.1	5.5	5.2	6.1	6.8	4.9	5.0	4.2	3.5	6.0	3.0	11.6	9.2	11.9	9.5	10.2	8.5
ICP-MS	Li	µg/g	4.22	4.68	2.42	3.78	2.90	3.20	6.51	4.54	2.80	2.33	3.63		1.38	0.27	1.10	0.39	
	Be	µg/g	0.04	0.01	0.03	0.02	b.d.	0.04	0.04	0.02	0.01	0.02	0.03		0.03	0.05	0.12	0.04	
	Sc	µg/g	14	14	14	13	9	16	16	13	11	14	11		12	14	16	14	
	V	µg/g	68	67	58	53	50	73	85	71	35	76	55		54	64	74	75	
	Co	µg/g	129	109	104	115	116	104	109	114	132	122	128		105	96	99	100	
	Ni	µg/g	2012	1963	2021	2050	2510	1858	1940	1962	2349	2140	2043		2116	1833	1764	1910	
	Cu	µg/g	8	9	5	17	122	14	11	4	2	19	3		31	42	34	24	
	Ga	µg/g	3	2	3	1	1	3	3	3	1	3	3		2	3	3	3	
	Zn	µg/g	56.97	49.84	50.96	47.59	51.71	50.28	48.56	48.83	51.79	49.71	62.03		60.10	51.87	49.70	49.42	
	Rb	µg/g	0.20	0.14	0.12	0.24	0.16	0.16	0.97	0.24	0.04	0.19	0.07		0.02	0.08	0.02	b.d.	
	Sr	µg/g	22	9	14	11	2	13	23	14	6	8	12		15	26	23	5	
	Y	µg/g	3.6	2.1	3.0	1.4	0.2	4.4	3.8	3.1	0.5	2.2	2.9		0.8	2.8	5.1	3.1	
	Zr	µg/g	3	2	2	2	1	2	1	1	1	2	2		b.d.	1	3	2	
	Cs	µg/g	0.03	0.03	0.03	0.03	0.01	0.02	0.09	0.02	0.01	0.02	0.01		0.01	0.09	0.03	0.03	
	Ba	µg/g	0.3	0.5	0.2	0.6	0.2	0.3	0.9	0.3	0.4	0.4	0.2		1.1	0.7	12.1	0.2	
	La	µg/g	0.13	0.22	0.13	0.17	0.13	0.14	0.20	0.11	0.07	0.14	0.14		0.09	0.17	0.25	0.13	
	Ce	µg/g	0.5	0.7	0.5	0.5	0.3	0.6	0.7	0.4	0.2	0.4	0.5		0.2	0.6	0.9	0.5	
	Pr	µg/g	0.10	0.10	0.09	0.08	0.03	0.12	0.13	0.08	0.03	0.07	0.09		0.03	0.11	0.17	0.10	
	Nd	µg/g	0.6	0.5	0.5	0.4	0.1	0.7	0.7	0.5	0.1	0.4	0.5		0.1	0.6	1.0	0.6	
	Sm	µg/g	0.26	0.16	0.22	0.10	0.02	0.30	0.28	0.21	0.02	0.14	0.21		0.03	0.21	0.39	0.23	
	Eu	µg/g	0.11	0.07	0.10	0.05	b.d.	0.13	0.11	0.09	0.02	0.06	0.09		0.01	0.07	0.16	0.08	
	Gd	µg/g	0.41	0.24	0.34	0.15	0.02	0.49	0.44	0.35	0.03	0.24	0.33		0.07	0.33	0.61	0.37	
	Tb	µg/g	0.08	0.04	0.06	0.03	b.d.	0.09	0.08	0.07	0.01	0.04	0.06		0.01	0.06	0.11	0.07	
	Dy	µg/g	0.5	0.3	0.4	0.2	b.d.	0.6	0.6	0.5	0.1	0.3	0.4		0.1	0.4	0.8	0.5	
	Ho	µg/g	0.119	0.072	0.100	0.045	0.006	0.146	0.123	0.103	0.015	0.071	0.097		0.028	0.093	0.172	0.107	
	Er	µg/g	0.34	0.21	0.29	0.14	0.02	0.42	0.36	0.30	0.05	0.21	0.28		0.09	0.27	0.48	0.30	
	Yb	µg/g	0.3	0.2	0.3	0.1	b.d.	0.4	0.4	0.3	0.1	0.2	0.3		0.1	0.3	0.5	0.3	
	Lu	µg/g	0.06	0.04	0.05	0.02	0.01	0.06	0.06	0.05	0.01	0.04	0.05		0.02	0.05	0.07	0.05	
	Hf	µg/g	0.13	0.06	0.10	0.07	0.02	0.11	0.08	0.08	0.02	0.08	0.07		0.01	0.04	0.10	0.07	
	Pb	µg/g	0.06	0.22	0.02	0.11	0.08	0.02	0.31	0.05	0.07	0.08	0.02		0.58	0.66	0.61	0.63	
	Th	µg/g	b.d.	0.02	b.d.	0.01	0.02	b.d.	0.02	0.01	b.d.	0.01	0.01		0.01	0.01	0.01	b.d.	
	U	µg/g	0.002	0.003	0.003	0.006	0.004	0.001	0.005	0.002	0.002	0.004	0.002		0.010	0.017	0.019	0.003	
	TiO_2	wt.%	0.13	0.05	0.10	0.05	0.02	0.14	0.19	0.13	0.02	0.15	0.09		0.04	0.12	0.17	0.15	
PGNAA	B	µg/g	3.24	2.37	3.60	1.82	2.39	2.44	4.03	2.92	2.08	2.78	2.41		3.17	2.76	6.85	10.20	
	S	µg/g	b.d.	b.d.	b.d.	b.d.	b.d.	b.d.	b.d.	b.d.	b.d.	b.d.	b.d.		846	748	522	525	
	Cl	µg/g	17	9	38	b.d.	28	44	13	28	19	b.d.	20		23	32	21	b.d.	
	H_2O	wt.%	4.9	6.3	6.0	6.8	7.5	5.7	5.8	5.1	4.2	7.0	4.0		9.6	11.0	9.8	10.7	
MS	δD_{SMOW}	‰	−89	−53	−39			−30	−49	−49		−56			−61	−112	−87		
	$\delta^{18}O_{SMOW}$	‰	4.7	5.2	5.2			4.5		4.7					4.9	4.9	4.1		

Serp = serpentinite and Ophi = ophicarbonate. LOI = Loss On Ignition. Mg# calculated as (MgO/40.3)/[(MgO/40.3) + (0.8998 * Fe2O3/74.85)]. *D* (m) = nearest orthogonal distance to the ophicarbonate – metabasite contact. Lat N = latitude North (Swiss coordinates), Long E = longitude East (Swiss coordinates). b.d. = below detection limit.

their mineral modes. The transition between these two types is gradual from the core to the rim of the massif. The first type is weakly deformed serpentinite (Figs. 2, 3, 4A–B) and represents >95% of the ultramafic massif (Fig. 2). In this rock type, carbonate is absent and diopside is rare (Table 1). The second type is ophicarbonate (Figs. 2 and 3), which is intensely deformed and shows a well-developed foliation (Fig. 4E). This rock is characterized by the presence of carbonate, and was observed in three localities in contact with the serpentinite (Figs. 2–3), where it has a few meters width. In all the studied samples, the serpentine mineral is antigorite (checked by micro-Raman, C. Groppo personal communication). Between the ophicarbonate and the Monte Leone gneiss, a 2 to 5 m thick metabasite can be observed. This metabasite is composed of various rock types with variable mineralogy, and sometimes shows intense deformation. The contact between the metabasite and the gneiss is tectonic and sharp. In contrast, ophicarbonate boudins are often found in the metabasite, suggesting that this contact is rather primary than tectonic (Keusen, 1972). Chemical compositions of the main minerals (major elements) can be found in Tables A to F in Appendix A.

4.1. Serpentinite

The serpentinite is a forsterite–tremolite–antigorite fels, sometimes containing diopside (Fig. 4A, C, D; Table 1), a typical assemblage in hydrated peridotites metamorphosed under amphibolite facies conditions (Evans and Trommsdorff, 1970). The assemblage forsterite +

Table 3
Whole rock composition of metabasite and gneiss

		Rock	Metabas	Metabas	Metabas	Gneiss	Gneiss	Gneiss
		Sample	G30A	G30B	G34	G32A	G32B	G36
		D (m)	−1	−2	−1	−10	−15	−8
		Lat N	113314	133314	132098	133314	133314	132098
		Long E	661834	661834	663142	661834	661834	663142
Method	Element	Unit						
XRF	SiO_2	wt.%	39.79	41.81	43.78	70.86	70.57	72.12
	TiO_2	wt.%	1.38	1.10	1.38	0.49	0.42	0.66
	Al_2O_3	wt.%	18.85	15.23	17.20	15.40	16.01	12.57
	Cr_2O_3	wt.%	0.06	0.06	0.05	b.d.	0.00	0.01
	Fe_2O_3	wt.%	11.33	10.97	10.88	3.23	2.53	5.38
	MnO	wt.%	0.17	0.18	0.19	0.04	0.04	0.12
	MgO	wt.%	11.61	13.32	9.75	1.18	0.79	1.93
	CaO	wt.%	16.03	15.85	15.79	1.62	2.18	4.56
	Na_2O	wt.%	1.46	1.88	1.57	2.91	3.25	3.16
	K_2O	wt.%	b.d.	b.d.	0.19	4.40	4.63	0.15
	Mg#		0.68	0.71	0.65	0.43	0.39	0.43
	LOI	wt.%	3.7	3.4	1.3	1.2	0.8	0.5
ICP-MS	Li	µg/g	14.36	12.00	11.66	36.28		7.22
	Be	µg/g	0.86	0.80	0.79	3.07		4.06
	Sc	µg/g	41	37	34	8		10
	V	µg/g	245	226	224	36		85
	Co	µg/g	83	77	69	81		83
	Ni	µg/g	257	237	245	14		31
	Cu	µg/g	6	5	5	10		11
	Ga	µg/g	20	19	18	30		18
	Zn	µg/g	49.22	45.00	70.12	55.90		58.35
	Rb	µg/g	1.12	1.00	1.16	162.99		8.23
	Sr	µg/g	979	933	536	187		379
	Y	µg/g	28.9	27.8	25.9	47.2		27.6
	Cs	µg/g	b.d.	b.d.	0.04	5.46		0.15
	Ba	µg/g	3	2	5	940		30
	La	µg/g	2.69	2.40	3.84	39.28		29.77
	Ce	µg/g	9.2	8.6	10.9	83.4		61.6
	Pr	µg/g	1.69	1.57	1.87	10.14		7.44
	Nd	µg/g	9.0	8.7	9.4	37.6		27.6
	Sm	µg/g	3.01	2.92	2.98	8.15		5.55
	Eu	µg/g	1.72	1.68	1.20	1.32		1.11
	Gd	µg/g	4.08	4.00	3.93	8.08		5.22
	Tb	µg/g	0.72	0.71	0.68	1.36		0.83
	Dy	µg/g	4.7	4.6	4.4	8.0		4.6
	Ho	µg/g	1.016	1.000	0.929	1.661		0.928
	Er	µg/g	2.86	2.81	2.59	4.68		2.61
	Yb	µg/g	2.7	2.7	2.4	4.1		2.4
	Lu	µg/g	0.41	0.40	0.37	0.58		0.35
	Pb	µg/g	6.4	6.3	15.0	29.1		3.8
	Th	µg/g	0.1	0.1	0.2	15.4		11.5
	U	µg/g	0.03	0.04	0.07	3.03		2.42
	TiO_2	wt.%	1.459	1.318	1.153	0.460		0.590
PGNAA	B	µg/g	3.49		1.83	8.79		0.92
	Cl	µg/g	19		18	b.d.		20
	H_2O	wt.%	3.9		2.1	1.5		0.9

Metabas = metabasite. LOI = Loss On Ignition. b.d. = below detection limit.
Mg# calculated as (MgO/40.3)/[(MgO/40.3)+(0.8998*Fe2O3/74.85)]. *D* (m) = nearest orthogonal distance to the ophicarbonate – metabasite contact. Lat N = latitude North (Swiss coordinates), Long E = longitude East (Swiss coordinates).
Metabas = metabasite. *D* (m) = nearest orthogonal distance to the ophicarbonate–metabasite contact. Lat N = latitude North (Swiss coordinates), Long E = longitude East (Swiss coordinates).

tremolite + antigorite was mentioned for the first time in the Geisspfad ultramafic body by Preiswerk (1901) and described as a metamorphic assemblage by Keusen (1970). This assemblage results from partial dehydration of the serpentinite during the reaction antigorite + diopside = forsterite + tremolite + fluid at approximately 0.6–0.7 GPa and 520–560 °C (Pastorelli et al., 1995). In the centre of the massif, most samples are diopside-free (Table 1) and contain the prograde assemblage antigorite + forsterite + tremolite. However, in other samples two types of diopside can be distinguished (Fig. 4C–D). The first type (Di_I) is preserved as a relict (≤500 μm) in a single sample (G27; Fig. 4D), where chlorite crystallized after its former cleavages or exsolutions (?) creating a ghost crystal. The second type of diopside (Di_{II}) has a very different aspect (Fig. 4C) compared to the first type. It is commonly found in serpentinite from the outer rim of the massif. This secondary diopside is smaller (≤200 μm) than the relic primary one. Modes and size of the different rock-forming minerals systematically change across the massif in the serpentinite (Table 1). Antigorite and diopside increase in abundance towards the rim of the massif (Table 1). The length of the tremolite needles is smaller than 200 μm in the centre of the body, but can reach 2 cm at the rim. Forsterite shows a maximum size of 1 mm in the centre and becomes smaller at the rim of the massif.

No systematic major element variation was observed between minerals from the centre and from the rim of the massif. Antigorite has Mg# from 0.93 to 0.94, Al_2O_3 contents of ~3.00 wt.% and Cr_2O_3 between 0.10 and 1.00 wt.%. Forsterite Mg# varies from 0.845 to 0.890. Its Ni content is comparable to those of olivine in the oceanic mantle (Allan and Dick, 1996), but its Mg# is lower (Arai, 1994). Amphibole is a nearly stoichiometric tremolite, and is zoned, with an increase of Ca and Si, and a decrease of Al, Na and K towards the rim. Diopside has a

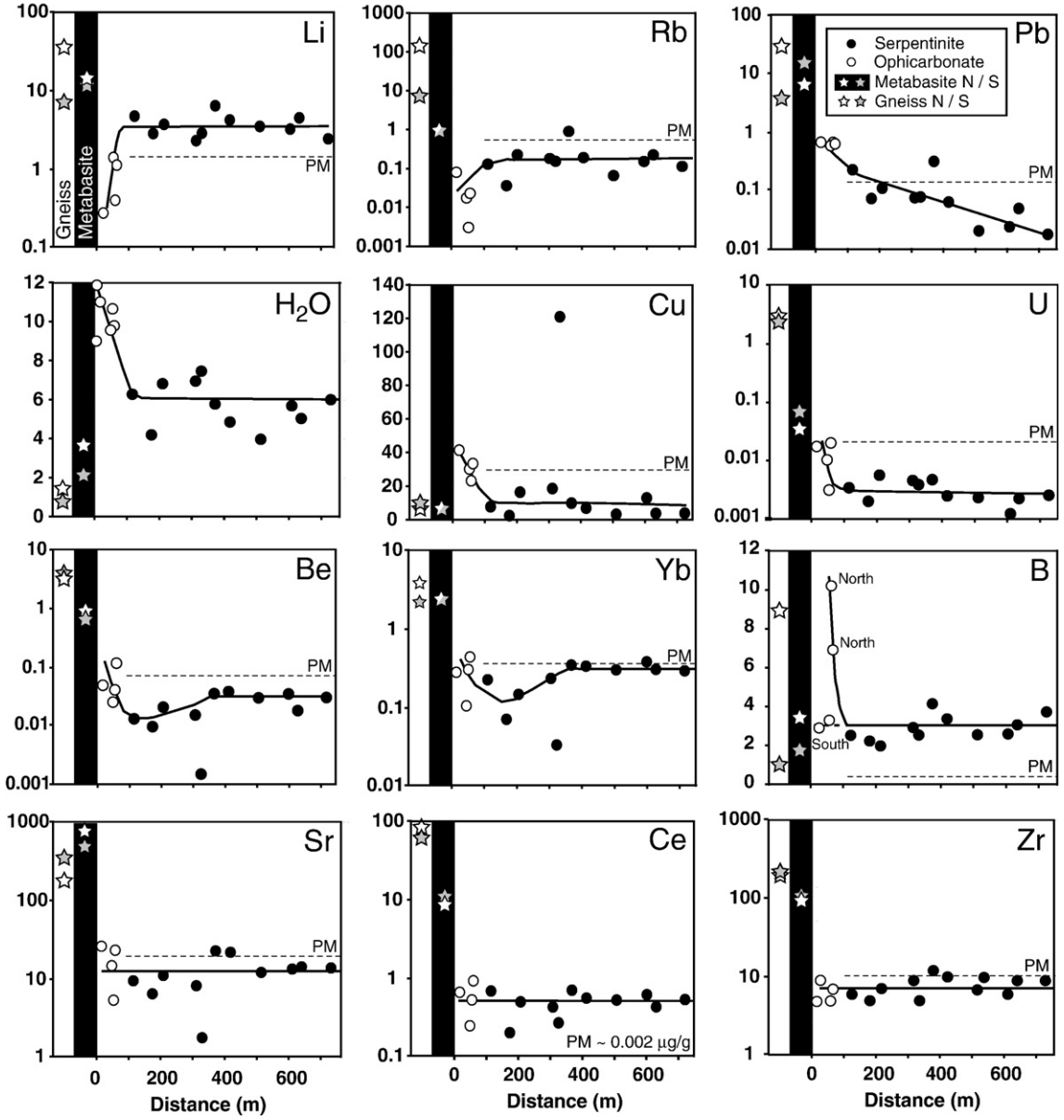

Fig. 5. Light, major and some trace elements (given in μg/g, except for H_2O given in wt.%) in whole rock samples of serpentinite, ophicarbonate, metabasite and Monte Leone gneiss. The various elements are subdivided into three groups depending on their behaviour through the ultramafic massif. First group: Li and Rb decrease towards the ophicarbonate–metabasite contact; second group: Pb, H_2O, Cu, U, Be, Yb and B increase towards the contact; third group: Sr, Ce and Zr remain more or less constant over the entire massif. Values for serpentinite and ophicarbonate are plotted relative to their nearest orthogonal distance to the ophicarbonate–metabasite contact (*x*-axis). For metabasite and gneiss, white stars represent samples from the northern contact (N; A on Figs. 2 or 3), and grey stars from the southern contact (S; A′ and B′ on Figs. 2 or 3). PM = primitive mantle (McDonough and Sun, 1995). Trend lines in black are eye-ball fits and were not calculated.

Cr_2O_3 content from below detection limit (<0.01 wt.%) up to 0.26 wt.%. Diopside from serpentinite is richer in Cr compared to diopside from ophicarbonate. Chlorite shows Cr_2O_3 contents between 0.04 and 2.25 wt.%. Chlorite in the serpentinite is generally enriched in Cr compared to chlorite from the ophicarbonate.

4.2. Ophicarbonate

Antigorite-rich ophicarbonates are strongly deformed and are found at the border of the ultramafic massif (Fig. 4E, G). The rock is a tremolite–antigorite schist with calcite and/or dolomite, with minor diopside and forsterite (Fig. 4E–H). The assemblage antigorite + calcite + tremolite can be observed in these rocks. Carbonate and diopside are not uniformly distributed in the samples, but are present in lenses (carbonate + antigorite + diopside + ilmenite + magnetite + Ni-rich sulphide), floating in an antigorite matrix (Fig. 4E–G). The assemblage antigorite + calcite + tremolite is found in these lenses, with abundant dolomite and diopside inclusions in tremolite (Fig. 4H). These lenses (up to 1 mm in diameter) are aligned along the foliation. Antigorite habits are different in the matrix (anhedral) and in the lenses (elongated needles).

Antigorite has Cr_2O_3 values between 0.09 and 0.31 wt.%. Its Cr content is generally lower than the Cr content of antigorite in serpentinite. Olivine (Fo_{89}) was found only in one sample (G3). Amphibole is a nearly stoichiometric tremolite, but lower in Na compared to the tremolite from serpentinite. Diopside has a Cr_2O_3 contents less than 0.09 wt.%. Calcite and dolomite both occur in the ophicarbonate, but in some cases calcite is the only carbonate present (sample GEI9). Calcite is nearly stoichiometric with up to 1.76 wt.% MgO while dolomite has a value around 17.0 wt.%, with substantial substitution of Mg by Fe.

4.3. Metabasite (contact)

The metabasic rocks observed at the contact between the gneiss and the ultramafic rocks are titanite–epidote–hornblende fels with chlorite (+/− calcite and grossular), dolomite–chlorite–tremolite fels, and chlorite–tremolite fels. In some rocks, amphibole can form needles up to several centimetres long, and can even be asbestiform. Grossular usually crystallized in veins in association with titanite and calcite. Samples containing chlorite + tremolite ± dolomite were found in the centre of the metabasite (Fig. 3). They presumably formed a metasomatic "blackwall" between the ultramafic rocks and the gneiss, as was shown in some New England ultramafic rocks by Sanford (1982).

The amphibole is a zoned tschermakitic hornblende with increasing Na_2O and Mg#, and decreasing K_2O towards the rim. Chlorite in metabasites is enriched in Al, Fe and Mn, and depleted in Ni, Cr and Mg compared to chlorite from serpentinite and ophicarbonate (Cr_2O_3 <0.10 wt.%, Mg# from 0.750 to 0.820). Titanite has Al_2O_3 and Fe_2O_3 contents of ~1.50 and 0.80 wt.%, respectively. Calcite and dolomite are minor phases in the metabasite, but were never found together. Calcite is nearly stoichiometric (MgO <0.80 wt.%). Dolomite has MgO content of ~21.0 wt.%, and has higher FeO content (~1.95 wt.%) compared to calcite.

5. Whole rock composition

Whole rock contents of major, light (Li, Be and B) and other trace elements were determined in the Geisspfad ultramafic rocks, as well as in the metabasite (contact) and in the Monte Leone gneiss. The results are listed in Tables 2 and 3, and are plotted in Figs. 5 and 6.

5.1. Serpentinite and ophicarbonate

In terms of major element contents (SiO_2, Al_2O_3, Fe_2O_3, MgO, CaO), serpentinites and ophicarbonates are similar to orogenic, ophiolitic and abyssal peridotites (Bodinier and Godard, 2004) (Table 2, Fig. A in Appendix A). Some major and trace elements display systematic variations across the massif (Fig. 5), and can be subdivided into three groups. All groups show more or less constant concentrations in the centre of the massif (except for Pb). The first group is represented by Li and Rb, which show a decrease in the ophicarbonate compared to the serpentinite. The second group includes Pb, H_2O, Cu, U, Be, Yb and B, which all increase at the rim of the massif. Strontium, Ce, and Zr are in the third group, with their concentrations more or less constant throughout the entire massif (Fig. 5).

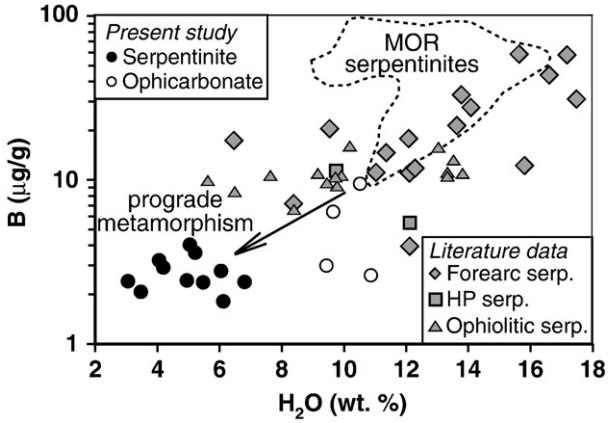

Fig. 6. B (µg/g) versus H_2O (wt.%) diagram of whole rock samples of serpentinite and ophicarbonate. Data from mid-ocean ridge (MOR), forearc, ophiolitic and high pressure serpentinites are plotted for comparison. MOR serpentinites: ODP Leg 209 after Vils et al. (submitted), Romanche and Vema fracture zones after Bonatti et al. (1984), Atlantis Massif after Boschi et al. (2008). Forearc serpentinites: Mariana Forearc ODP Leg 125 after Savov et al. (2005). Ophiolitic serpentinites: Feather River Ophiolite, California (USA) after Agranier et al. (2007). High pressure serpentinites: Syros (Greece) after Marschall (2005).

Lithium strongly decreases towards the margin from ~4.0 µg/g in the serpentinite to <1.5 µg/g in the ophicarbonate (Fig. 5). The values in the serpentinite are comparable to South West Indian ridge serpentinites (mean value ~3.5 µg/g; Decitre et al., 2002), and the ophicarbonate to Mid-Atlantic ridge serpentinites (mean value ~0.7 µg/g; Vils et al., submitted). Rubidium in the serpentinite shows values similar to that of the primitive mantle (McDonough and Sun, 1995).

The behaviour of Pb is unique, as it is characterized by a continuous increase all through the ultramafic massif, which can be observed over a distance of ~800 m. Beryllium and ytterbium show a decrease within the serpentinite, and then an increase in the ophicarbonate. Beryllium concentrations (<0.06 µg/g; Fig. 5) are slightly lower than the primitive mantle value ~0.068 µg/g (McDonough and Sun, 1995). Boron content in serpentinite is about 3 µg/g, with the exception of the northern contact (~10 µg/g, samples GEI9 and G13; Figs. 2, 3 and 5 i). The boron content in the centre is about three times lower than the minimum mid-ocean ridge serpentinite value of about 10 µg/g (Fig. 6; Bonatti et al., 1984; Boschi et al., 2008; Vils et al., submitted). Boron contents in the serpentinite are usually lower than values in high pressure serpentinite from Syros (5.5–11.3 µg/g; Marschall, 2005; Fig. 6). The characteristic increase of the trace elements from the second group (except for Pb) is localized within about 100 m from the contact in the ophicarbonate zone.

In the third group, Sr values in the centre of the massif are similar to the primitive mantle value (McDonough and Sun, 1995), while Ce content in serpentinite and ophicarbonate is 100 times higher than the primitive mantle value.

5.2. Metabasite (contact) and Monte Leone gneiss

Three metabasites and two gneisses were analyzed (Table 3, Fig. 5). Metabasite shows rare earth element (REE) patterns (Fig. B in Appendix A) comparable to normal mid-ocean ridge basalt (N-MORB).

Lithium, beryllium, and boron contents in the metabasite are ~13 μg/g, ~0.8 μg/g and ~2.5 μg/g, close to values of N-MORB.

The REE pattern of the gneiss shows a strong fractionation between the light and the heavy REE with La_N/Yb_N of 6.5 and 8.4 (Fig. B from Appendix A). Lithium, beryllium, and boron contents of the two gneisses are 7 and 36 μg/g, 0.9 and 8.8 μg/g, and 3.1 and 4.1 μg/g, respectively. These values are comparable to data of the continental crust (Li: 11–18 μg/g, Be: 1.5–2.4 μg/g, B: 10–18 μg/g; Rudnick and Fountain, 1995; Taylor and McLennan, 1995; Wedepohl, 1995; Gao et al., 1998).

5.3. Whole rock stable isotopic composition

Results are listed in Table 2 and shown in Fig. 7. $\delta^{18}O$ and δD values were measured in whole rock samples (serpentinite and ophicarbonate). $\delta^{18}O$ is constant through the Geisspfad massif, in serpentinite and ophicarbonate, with a mean value of +4.8‰. In contrast, δD values decrease from the centre to the rim of the massif from −30‰ to −112‰ (except for sample GEI4, which is off-trend with a value of − 89‰).

6. Mineral composition—light elements (Li, Be and B)

Light element contents of minerals were measured along two main profiles through the massif (A–A′ and B–B′, Figs. 2 and 3). Measurements from the serpentinite and ophicarbonate are presented together, because their mineralogical composition is similar. Results are shown in Table 4 and in Figs. 8 to 9.

6.1. Serpentinite and ophicarbonate

Lithium contents are highly variable in all minerals (Fig. C in Appendix A). Antigorite is poor in Li with values from <0.1 up to 4.0 μg/g. Sample GEI4 (~416 m from the contact), shows the greatest variability in Li contents of antigorite between 0.04 and 3.80 μg/g. Forsterite, tremolite and diopside have values of 1.7–10.1, 0.2–11.8 and 0.5–31.6 μg/g, respectively. Results for chlorite range from <0.1 up to 1.8 μg/g. Calcite and dolomite are poor in Li with values <0.2 μg/g.

The highest Be concentrations were measured in diopside (0.02–0.98 μg/g) and tremolite (0.04 and 0.29 μg/g). All the other minerals have Be contents <0.05 μg/g.

The major B-bearing phases are antigorite and tremolite, with contents ranging from 0.8 to 35.3, and 1.7 to 19.7 μg/g, respectively.

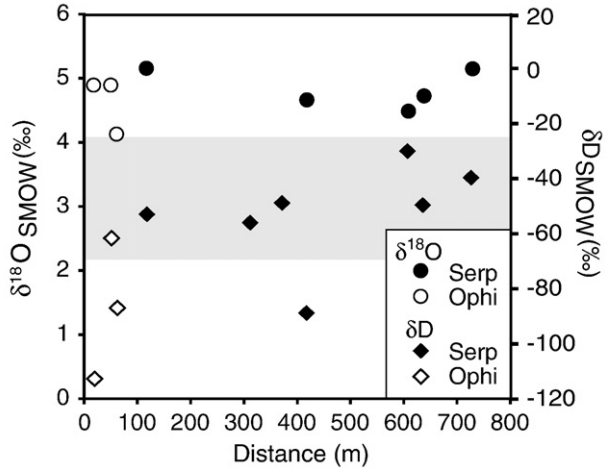

Fig. 7. Hydrogen and oxygen isotope ratios of whole rock samples of serpentinite and ophicarbonate. Grey field: δD of oceanic serpentine (mineral separates) after Wenner and Taylor (1974) and Früh-Green et al. (1996). $\delta^{18}O$ values of Geisspfad serpentinite and ophicarbonate are within the range of values published for oceanic serpentine ($\delta^{18}O$: 0 to 13‰; Wenner and Taylor, 1974; Früh-Green et al., 1996). The *x*-axis represents the orthogonal distance between the sample location and the nearest ophicarbonate–metabasite contact.

Table 4
Light element composition of minerals (representative analyses)

Rock	Sample	*N*	Min	Li (μg/g)	2σ	Be (μg/g)	2σ	B (μg/g)	2σ
Serp	GEI4	4	Atg	3.80	0.05	0.003	0.002	2.9	0.1
	GEI4		Atg	1.24	0.04	<0.001		1.48	0.07
	GEI4		Atg	0.04	0.02	0.002	0.002	2.52	0.08
	G11	6	Atg	0.08	0.01	0.002	0.001	2.0	0.1
	G11		Atg	0.21	0.01	0.007	0.002	2.43	0.07
	G11		Atg	0.18	0.02	0.004	0.002	2.78	0.08
	G12	6	Atg	0.17	0.04	0.006	0.002	5.0	0.1
	G12		Atg	0.020	0.004	<0.001		1.78	0.05
	G12		Atg	0.02	0.01	<0.001		0.75	0.06
	G26	5	Atg	0.10	0.01	<0.001		2.3	0.1
	G26		Atg	0.06	0.01	0.004	0.003	1.60	0.07
	G26		Atg	0.13	0.02	0.005	0.004	3.0	0.2
	G27	5	Atg	0.10	0.01	<0.002		1.64	0.09
	G27		Atg	0.02	0.01	<0.002		1.75	0.08
	G27		Atg	0.02	0.01	<0.002		1.36	0.09
Ophi	G3	5	Atg	0.05	0.01	0.018	0.007	1.99	0.08
	G3		Atg	0.03	0.01	0.008	0.003	1.50	0.06
	G3		Atg	0.02	0.01	0.009	0.005	2.6	0.1
	G4	5	Atg	0.10	0.01	0.030	0.006	7.5	0.3
	G4		Atg	0.08	0.02	0.020	0.008	2.38	0.08
	G4		Atg	0.11	0.01	0.023	0.006	3.3	0.2
	GEI9	6	Atg	0.27	0.02	0.029	0.005	35.3	0.9
	GEI9		Atg	0.51	0.02	0.040	0.006	25	1
	GEI9		Atg	0.25	0.02	0.019	0.003	10.1	0.4
	GEI9		Atg	0.42	0.02	0.015	0.002	4.8	0.1
Serp	G11	5	Di II	31.6	0.3	0.13	0.02	0.39	0.04
	G11		Di II	27.4	0.3	0.11	0.01	0.15	0.03
	G11		Di II	2.27	0.07	0.016	0.008	0.67	0.04
	G11		Di II	9.1	0.2	0.13	0.01	0.06	0.02
	G26	5	Di II	11.8	0.1	0.05	0.01	0.33	0.03
	G26		Di II	7.5	0.1	0.025	0.008	0.23	0.03
	G26		Di II	13.3	0.3	0.03	0.01	0.28	0.05
	G27	3	Di II	1.23	0.04	0.027	0.008	1.1	0.1
	G27		Di II	0.71	0.05	0.025	0.008	0.48	0.07
	G27		Di II	0.89	0.05	0.022	0.007	0.52	0.05
Ophi	G4	5	Di II	0.65	0.03	0.67	0.04	1.62	0.09
	G4		Di II	0.80	0.05	0.98	0.05	2.2	0.1
	G4		Di II	0.81	0.04	0.51	0.04	1.4	0.1
	GEI9	6	Di II	1.19	0.03	0.121	0.006	0.85	0.06
	GEI9		Di II	1.29	0.02	0.127	0.009	0.99	0.04
	GEI9		Di II	0.52	0.02	0.32	0.01	1.16	0.04
Serp	GEI4	7	Tr	1.59	0.05	0.082	0.005	11.5	0.2
	GEI4		Tr	2.01	0.07	0.099	0.006	12.51	0.08
	GEI4		Tr	2.75	0.07	0.12	0.01	11.8	0.2
	G11	7	Tr	7.16	0.05	0.068	0.006	4.4	0.1
	G11		Tr	9.8	0.1	0.079	0.004	9.5	0.1
	G11		Tr	11.6	0.1	0.14	0.01	18.2	0.2
	G12	6	Tr	0.63	0.04	0.163	0.007	9.2	0.2
	G12		Tr	0.40	0.02	0.090	0.008	8.0	0.3
	G12		Tr	0.81	0.03	0.19	0.01	12.0	0.2
	G26	8	Tr	9.1	0.1	0.13	0.02	6.4	0.2
	G26		Tr	10.4	0.1	0.15	0.02	4.6	0.2
	G26		Tr	5.4	0.1	0.14	0.02	7.3	0.2
	G26		Tr	5.55	0.07	0.10	0.02	13.6	0.3
	G27	10	Tr	5.1	0.1	0.13	0.02	13.9	0.3
	G27		Tr	3.42	0.08	0.05	0.01	4.2	0.1
	G27		Tr	3.19	0.08	0.09	0.01	7.5	0.2
	G27		Tr	2.10	0.07	0.07	0.02	4.2	0.2
	G27		Tr	3.34	0.07	0.16	0.02	19.7	0.4
	G27		Tr	1.85	0.05	0.06	0.01	3.1	0.1
Ophi	G3	10	Tr	2.79	0.07	0.17	0.02	5.7	0.2
	G3		Tr	1.85	0.07	0.13	0.02	4.2	0.1
	G3		Tr	2.34	0.05	0.29	0.03	8.2	0.3
	G3		Tr	0.70	0.06	0.06	0.02	1.64	0.09
	G4	9	Tr	0.49	0.04	0.054	0.008	2.0	0.1
	G4		Tr	0.71	0.04	0.069	0.007	3.3	0.1
	G4		Tr	0.45	0.03	0.09	0.02	3.6	0.1
	G4		Tr	0.48	0.03	0.05	0.01	2.1	0.1
	GEI9	7	Tr	0.25	0.01	0.107	0.006	3.7	0.1
	GEI9		Tr	0.37	0.03	0.092	0.007	4.44	0.07
	GEI9		Tr	0.19	0.02	0.080	0.008	2.8	0.1
Metabas	G30a	5	Hbl	2.51	0.04	2.10	0.05	7.7	0.2
	G30a		Hbl	2.31	0.05	1.51	0.03	6.8	0.1
	G30a		Hbl	1.76	0.06	1.03	0.03	5.1	0.1
	G34	5	Hbl	9.3	0.1	0.59	0.02	1.99	0.09

Table 4 (*continued*)

Rock	Sample	*N*	Min	Li (μg/g)	2σ	Be (μg/g)	2σ	B (μg/g)	2σ
Metabas	G34		Hbl	8.4	0.2	0.66	0.02	1.8	0.1
	G34		Hbl	11.5	0.2	0.75	0.02	2.30	0.09
Serp	GEI4	8	Fo	6.07	0.08	<0.001		0.13	0.02
	GEI4		Fo	5.88	0.09	0.002	0.002	0.35	0.02
	GEI4		Fo	6.49	0.09	<0.001		0.16	0.03
	GEI4		Fo	4.1	0.2	<0.001		0.60	0.04
	G11	12	Fo	8.8	0.1	<0.001		4.70	0.09
	G11		Fo	6.52	0.09	<0.001		3.24	0.07
	G11		Fo	4.57	0.07	<0.001		3.5	0.1
	G11		Fo	6.9	0.1	<0.001		5.6	0.1
	G11		Fo	6.45	0.05	<0.001		0.24	0.02
	G11		Fo	3.81	0.06	<0.001		4.7	0.1
	G11		Fo	4.56	0.05	<0.001		1.21	0.06
	G11		Fo	10.1	0.1	<0.001		7.8	0.1
	G12	6	Fo	3.90	0.07	<0.001		0.24	0.03
	G12		Fo	3.67	0.04	<0.001		0.29	0.02
	G12		Fo	3.86	0.06	<0.001		0.21	0.02
	G26	9	Fo	2.08	0.05	<0.001		0.11	0.02
	G26		Fo	1.66	0.06	<0.001		0.11	0.02
	G27	5	Fo	5.5	0.1	<0.002		0.9	0.1
	G27		Fo	5.6	0.1	<0.002		0.81	0.08
Ophi	G3	10	Fo	3.61	0.08	0.002	0.002	2.9	0.1
	G3		Fo	4.4	0.1	<0.002		2.29	0.09
	G3		Fo	3.5	0.1	0.002	0.002	3.6	0.2
Serp	GEI4	7	Chl	0.10	0.02	0.002	0.001	1.68	0.08
	GEI4		Chl	0.39	0.02	<0.001		0.7	0.2
	GEI4		Chl	0.12	0.02	0.002	0.001	1.3	0.2
	GEI4		Chl	0.13	0.03	<0.001		2	1
	G11	6	Chl	0.45	0.02	0.002	0.001	1.28	0.05
	G11		Chl	0.60	0.02	0.005	0.002	2.1	0.1
	G11		Chl	0.44	0.02	0.004	0.001	0.69	0.03
	G11		Chl	0.54	0.02	0.005	0.001	1.59	0.08
	G12	6	Chl	0.07	0.01	<0.001		1.3	0.1
	G12		Chl	0.12	0.01	0.002	0.001	2.0	0.2
	G12		Chl	0.09	0.01	0.005	0.002	3.1	0.1
	G12		Chl	0.03	0.01	<0.001		1.09	0.04
	G26	4	Chl	0.21	0.02	0.002	0.002	1.0	0.1
	G26		Chl	0.23	0.02	<0.001		0.86	0.05
	G26		Chl	0.20	0.02	<0.001		1.10	0.06
	G27	5	Chl	0.04	0.01	<0.002		0.87	0.08
	G27		Chl	0.04	0.01	0.004	0.003	1.27	0.08
	G27		Chl	0.05	0.01	0.003	0.002	1.12	0.07
Ophi	GEI9	6	Chl	1.35	0.04	0.022	0.003	1.3	0.1
	GEI9		Chl	1.46	0.04	0.022	0.003	1.4	0.1
	GEI9		Chl	1.46	0.04	0.035	0.004	2.13	0.09
Metabas	G30a	4	Chl	27.6	0.1	0.013	0.002	0.7	0.1
	G30a		Chl	33.0	0.2	0.024	0.005	0.8	0.1
	G30a		Chl	33.4	0.4	0.019	0.005	2.0	0.3
	G34	5	Chl	75.2	0.9	0.021	0.003	2.0	0.3
	G34		Chl	65.5	0.4	0.021	0.003	0.8	0.2
	G34		Chl	62.9	0.5	0.021	0.005	0.31	0.06
	G34		Chl	63.7	0.7	0.223	0.009	1.5	0.1
Metabas	G30a	4	Ep	0.08	0.02	0.028	0.005	1.6	0.1
	G30a		Ep	0.82	0.02	0.025	0.004	1.22	0.06
	G30a		Ep	0.019	0.005	0.021	0.004	1.74	0.08
	G34	5	Ep	0.09	0.01	0.008	0.004	0.17	0.03
	G34		Ep	0.10	0.01	0.008	0.001	0.03	0.01
	G34		Ep	0.15	0.02	0.029	0.005	0.09	0.02
Metabas	G30a	3	Ttn	0.07	0.01	0.097	0.007	1.38	0.08
	G30a		Ttn	0.55	0.06	0.076	0.005	0.98	0.06
	G30a		Ttn	0.80	0.04	0.115	0.009	0.74	0.03
	G34	3	Ttn	3.78	0.06	0.41	0.01	0.88	0.06
	G34		Ttn	3.97	0.07	0.28	0.02	0.75	0.07
	G34		Ttn	0.02	0.01	0.04	0.01	0.20	0.03
Ophi	G3	5	Cal	0.020	0.004	<0.001		0.11	0.01
	G3		Cal	0.05	0.01	<0.001		0.05	0.02
	G3		Cal	0.008	0.002	<0.001		0.09	0.01
	G4	4	Cal	0.019	0.002	0.010	0.002	0.12	0.01
	G4		Cal	0.022	0.001	0.016	0.001	0.18	0.01
	G4		Cal	0.018	0.001	0.015	0.001	0.12	0.01
	GEI9	4	Cal	0.03	0.01	<0.001		0.12	0.02
	GEI9		Cal	0.006	0.001	<0.001		0.12	0.02
Ophi	G3	4	Dol	0.08	0.01	<0.001		0.15	0.01
	G3		Dol	0.026	0.004	<0.001		0.08	0.01
	G3		Dol	0.023	0.003	<0.001		0.08	0.01

Table 4 (*continued*)

Rock	Sample	*N*	Min	Li (μg/g)	2σ	Be (μg/g)	2σ	B (μg/g)	2σ
Ophi	G4	5	Dol	0.171	0.004	<0.001		0.084	0.003
	G4		Dol	0.111	0.004	<0.001		0.068	0.002
	G4		Dol	0.026	0.001	<0.001		0.08	0.01

N = total number of analysis. Abbreviations: Cal = calcite, Chl = chlorite, Dol = dolomite, Ep = epidote, Fo = forsterite, Ttn = titanite. Serp = serpentinite, Ophi = ophicarbonate, Metabas = metabasite.

N = total number of analysis. Abbreviations: Atg = antigorite, Di II = secondary diopside, Hbl = tschermakitic hornblende, Tr = tremolite. Serp = serpentinite, Ophi = ophicarbonate, Metabas = metabasite.

Forsterite (0.1 to 7.8 μg/g) and diopside (<0.1 to 2.4 μg/g) have lower B contents. Chlorite may contain up to 3.1 μg/g of B, while calcite and dolomite have values <0.2 μg/g.

In a cross section through the Geisspfad massif, Li contents of tremolite, antigorite and diopside increase in the serpentinite towards the rim of the massif and then decrease in the ophicarbonate (Fig. 8). In contrast, Li contents of forsterite stay constant through the massif (Fig. 8). A progressive increase in Be from the serpentinite to the ophicarbonate is observed in antigorite and diopside, but not in tremolite (Fig. 8). Boron content also slightly increases from the serpentinite to the ophicarbonate in forsterite and diopside (Fig. 8). In contrast, B in tremolite is constant in the serpentinite and decreases in the ophicarbonate (Fig. 8).

Fig. 9 illustrates the mean content of Li, Be, and B in minerals from serpentinite and ophicarbonate. The distribution of each light element between the minerals of the assemblage antigorite + diopside + tremolite + forsterite is similar in the samples from the centre of the massif (Fig. 9, Table 5). In contrast, for all three light elements this distribution varies near to the contact in the serpentinite and in the ophicarbonate (Fig. 9), up to a distance of approximately 150 m. In the centre of the massif, forsterite shows the highest Li contents, while Be and B are concentrated in tremolite (Fig. 9). The beryllium concentration decreases in the order tremolite > diopside > antigorite > forsterite in the centre of the massif, while diopside has the highest Be contents at the rim of the massif (Fig. 9). For boron, the concentration decreases in the order tremolite > antigorite > forsterite > diopside in the centre of the massif, while antigorite sometimes contains more B than tremolite at the rim (Fig. 9).

6.2. Metabasite (contact)

The major Li carrier in metabasic rocks is chlorite (27.6 to 75.2 μg/g), followed by tschermakitic hornblende (up to 11.5 μg/g). Epidote is poor in Li (<0.8 μg/g), while titanite has values up to 4.0 μg/g. Tschermakitic hornblende and chlorite have Be contents up to 2.1 and 0.2 μg/g, respectively. Tschermakitic hornblende has the highest B content, 7.7 μg/g, while chlorite has values between 0.3 and 2.0 μg/g. Epidote and titanite are both poor in Be (<0.400 μg/g) and B (<1.7 μg/g).

7. Discussion

7.1. Nature of the protolith

REE patterns of serpentinite fall into two groups (Fig. 10). Rocks from group I (Fig. 10) show a REE pattern with a flat HREE segment at 1 to 2× chondrite, and LREE fractionation (Ce_N/Sm_N = 0.48 to 0.99). This signature corresponds to fertile orogenic lherzolites (e.g., Bodinier and Godard, 2004). According to Pastorelli et al. (1995), the protolith of the Geisspfad serpentinite is a subcontinental spinel lherzolite, which evolved in an ocean–continent transition environment during rifting. The REE pattern of group I serpentinites is in agreement with this hypothesis, but it could also correspond to slightly depleted subcontinental mantle.

Rocks from group II (G15 and G26) are characterized by a U-shaped REE pattern (Fig. 10), with fractionation of both light REE (Ce_N/Sm_N = 1.75 to 3.50), and heavy REE (Gd_N/Lu_N = 0.33 to 0.42).

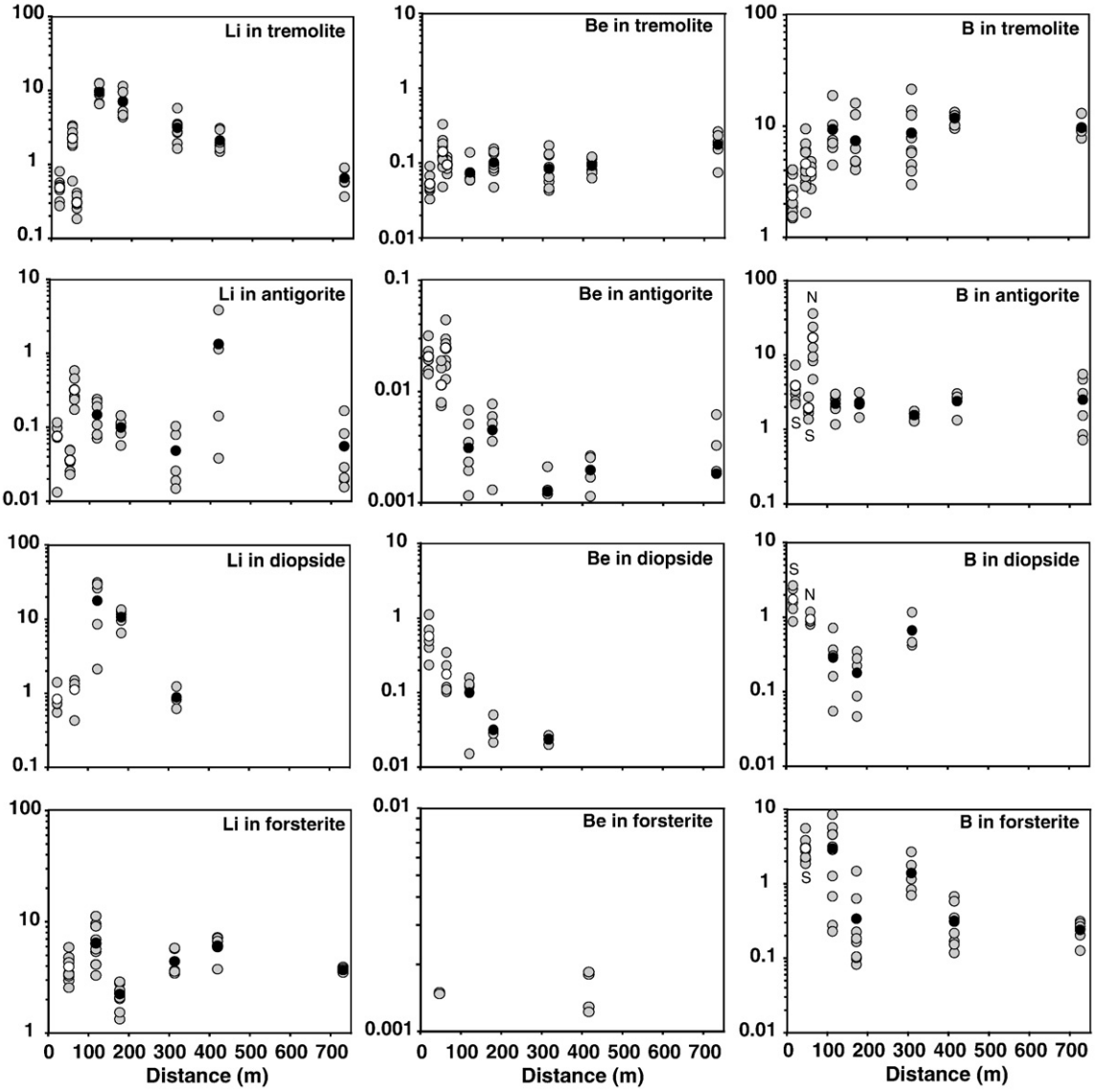

Fig. 8. Li, Be, and B content of minerals (in μg/g) in serpentinite and ophicarbonate as a function of their nearest orthogonal distance to the ophicarbonate–metabasite contact (*x*-axis). Grey circles represent single measurements. Black circles are average values for serpentinite, and white circles are average values for ophicarbonate. N: northern contact, S: southern contact. Be content of forsterite was usually below detection limit (<0.001 μg/g), except for the 4 analyses represented in this diagram (for this reason no average data are presented). Relative standard deviation (2σ) for Li ranges between 0.01 and 0.11 μg/g, for Be between 0.001 and 0.210 μg/g, and for B between 0.06 and 0.20 μg/g.

The concentration of REE in whole rock samples of group II is approximately one order of magnitude lower than for group I. Group II samples (G15, G26) have higher MgO and lower Al_2O_3 and Y contents compared to serpentinites from group I (Fig. A in Appendix A; Table 2). REE patterns similar to group II are usually attributed to zones of melt percolation in fertile lherzolites (Bodinier and Godard, 2004), and are comparable to those observed in Huinan spinel harzburgite (Xu et al., 2003), which reacted with basaltic melts. For these reasons, the protolith of samples G15 and G26 is probably a dunite.

7.2. Serpentinization of the protolith

Metarodingites and serpentinites are present in the Geisspfad massif. This rock association was described in the present-day Iberia Abyssal Plain (Boillot et al., 1980), but also in Mesozoic ocean–continent transitions of the Alps (Platta-Val Malenco transect, Swiss-Italian Alps; Manatschal and Nievergelt, 1997; Müntener et al., 2000) and the northern Apennines (Marroni et al., 1998). In the centre of the massif, the Geisspfad serpentinite shows hydrogen and oxygen whole rock isotopic composition (Fig. 7) similar to oceanic serpentine drilled or dredged on the ocean floor (Wenner and Taylor, 1974; Früh-Green et al., 1996; Boschi et al., 2008). On the other hand, some ophicarbonates near to the contact show strongly negative ∂D values (Fig. 7). Früh-Green et al. (1990) demonstrated that under similar metamorphic conditions, serpentine in ophicarbonate shows higher ∂D values than serpentine in serpentinites. As modal serpentine in the Geisspfad ophicarbonate exceeds 70% (Table 1), this mineral is likely to control the ∂D value of the bulk rock. According to Früh-Green et al. (1990), this would generate higher ∂D values in the ophicarbonate than in the serpentinite. Our observations show the opposite and we conclude that the ∂D decrease from the core to the rim of the Geisspfad massif is not related to a change in lithology. We propose that the low ∂D values resulted from a two-step fluid history: (i) A reaction between peridotite and a seawater-derived fluid, supported by the $\delta^{18}O$ and δD values of the Geisspfad serpentinite. The increase in Cu whole rock content (up to 42 μg/g) in the ophicarbonate could be related to hydrothermal activity on the ocean floor related to volcanism (Zierenberg et al., 1998), or hosted by

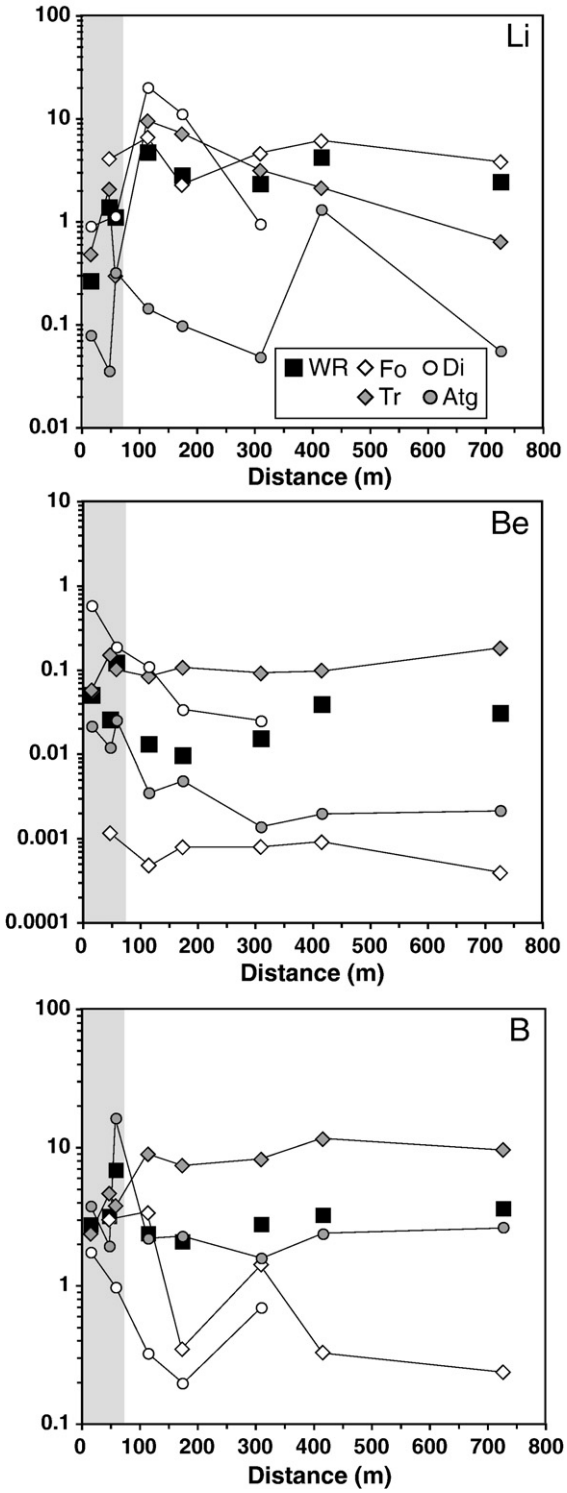

Fig. 9. Average lithium (Li), beryllium (Be) and boron (B) contents (in µg/g) in minerals and whole rock plotted relative to their nearest orthogonal distance to the ophicarbonate–metabasite contact (*x*-axis). This diagram illustrates the internal element redistributions between the coexisting minerals related to changes in modal composition and/or disequilibrium. Grey fields represent the ophicarbonate. Abbreviations: Atg = antigorite, Di = diopside, Fo = forsterite, Tr = tremolite, WR = whole rock.

peridotite as in the present-day Logatchev hydrothermal field (Cu in the fluid: 2.8 µg/g; Schmidt et al., 2007). (ii) A reaction between the ophicarbonate (at least) and a crust-derived fluid, supported by the decrease of the ∂D values towards the rim of the massif (Fig. 7). The increase of the Pb whole rock content within the entire Geisspfad body (Fig. 5) is probably related to the reaction between the ultramafic rocks and the crust-derived fluid.

Table 5
Distribution factor (calculated from mineral–mineral cores) of Li, Be and B between the coexisting phases of the texturally equilibrated samples from the centre of the massif

Element	Min/min	GEI4 average	1σ	G12 average	1σ	G27 average	1σ	All samples average	1σ
Li	Tr/Fo	0.4	0.1	0.17	0.04	0.6	0.2	0.3	0.2
	Tr/Di					3	1		
	Tr/Atg	18	23	23	14	107	83	54	68
	Atg/Di					0.06	0.05		
	Atg/Fo	0.2	0.3	0.01	0.01	0.01	0.01	0.1	0.2
	Fo/Di					6	1		
Be	Tr/Fo	175	134	500	196	114	44	261	215
	Tr/Di					4	1		
	Tr/Atg	26	19	235	248	76	46	125	168
	Atg/Di					0.06	0.02		
	Atg/Fo	3	2	6	4	1.6	0.8	4	3
	Fo/Di					0.03	0		
B	Tr/Fo	50	27	44	14	9	6	40	26
	Tr/Di					13	10		
	Tr/Atg	5	2	6	4	5	3	5	3
	Atg/Di					2.6	0.9		
	Atg/Fo	10	6	12	9	2.0	0.6	10	8
	Fo/Di					1.5	0.5		

In the serpentinite and ophicarbonate, the serpentine usually found in oceanic environments (lizardite and chrysotile) was transformed to antigorite during prograde Alpine metamorphism and recrystallization (e.g., Evans and Trommsdorff, 1970).

7.3. Li, Be, and B budgets of the protolith before Alpine metamorphism

The increase in Pb whole rock content (Fig. 5), and the shift in δD values (Fig. 7) at the rim of the ultramafic massif indicates interaction with crust-derived fluids. In contrast, the serpentinite (at least in the centre of the massif) seems to be almost unaffected by such fluids (Fig. 5). The serpentinite has an average Pb abundance (0.1 µg/g) lower than the primitive mantle (0.150 µg/g; McDonough and Sun, 1995). For this reason, when constraining the Li, Be, and B contents of the protolith of the Geisspfad body, the ophicarbonate should not be considered.

Partial dehydration of the Geisspfad serpentinite was driven by the reaction antigorite + diopside = forsterite + tremolite + fluid (0.6–0.7 GPa, 520–560 °C; Pastorelli et al., 1995). Scambelluri et al. (2004)

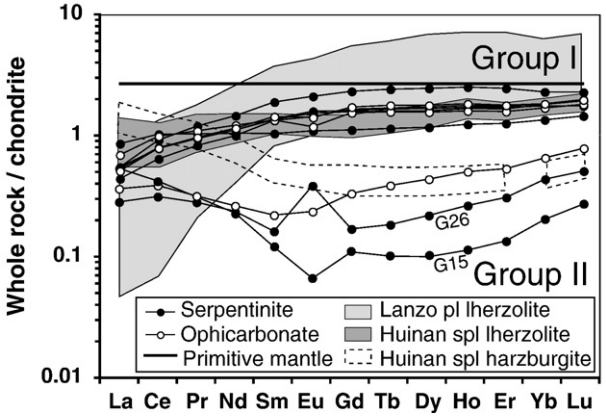

Fig. 10. Rare Earth Element (REE) compositions of the Geisspfad serpentinites and ophicarbonates. Primitive mantle after McDonough and Sun (1995). Huinan spinel lherzolite and harzburgite after Xu et al. (2003), and Lanzo plagioclase lherzolite after Müntener et al. (2005) and are plotted for comparison.

showed that Li is fairly immobile during serpentinite dehydration at high pressure (reaction: antigorite + brucite = forsterite + fluid). As diopside can contain up to ~5 µg/g of Li in oceanic serpentinites (Decitre et al., 2002; Pelletier et al., in review; Vils et al., accepted), its decomposition during prograde metamorphism could potentially liberate some Li into the fluid ($^{Li}D_{cpx\text{-}fluid}$ = 0.16 after Brenan et al., 1998b). The antigorite consumed during the reaction could have played a role, as Li content in antigorite from high pressure serpentinite ranges between 0.02 and 4.32 µg/g (Scambelluri et al., 2004; Marschall, 2005). However, some Li liberated during the reaction was probably stored in forsterite and tremolite, as shown by Scambelluri et al. (2004) for dehydration at high pressure. By analogy, the Li whole rock content of Geisspfad serpentinites probably decreased during prograde metamorphism, but this loss cannot be quantified. The whole rock Li content in Geisspfad serpentinite ranges from 2.3 to 6.5 µg/g. This value is similar to Li content in serpentinites from mid-ocean ridges (0.1–13.7 µg/g; Decitre et al., 2002; Niu, 2004; Vils et al., accepted), but higher than the value of 1.6 µg/g attributed to the primitive mantle by McDonough and Sun (1995). This indicates that little Li is incorporated in ultramafic rocks during serpentinization (Pelletier et al., in review; Vils et al., accepted). In conclusion, the Li content of the Geisspfad serpentinite is probably slightly lower than that of unmetamorphosed serpentinite precursor.

The beryllium content of the Geisspfad serpentinite varies between 0.01 and 0.04 µg/g, except for samples G15 and G26, which have lower values. Our unpublished results indicate that no Be is added during serpentinization, because Be content of serpentinites is silimar to the one of fresh oceanic peridotites (Pelletier et al., in review; Vils et al., accepted). Experiments and natural observations in basaltic systems suggest that Be is highly compatible during fluid production, with $^{Be}D_{cpx\text{-}fluid}$ = 1.8 (Brenan et al., 1998b) and $^{Be}D_{Ca\text{-}amphibole\text{-}fluid}$ = 4.14 (Marschall et al., 2007). By analogy, no Be should have been lost during prograde metamorphism, and Be content of the Geisspfad serpentinite should be representative of its protolith. The Geisspfad serpentinite has values lower than the primitive mantle (0.068 µg/g; McDonough and Sun, 1995), but similar to serpentinites from the Feather River ophiolite in California (Li and Lee, 2006) with values between 0.01 and 0.06 µg/g. Be is incompatible during melting of peridotite (Brenan et al., 1998a). For this reason, the lower Be content of the Geisspfad serpentinite compared to primitive mantle estimates can be explained by low degrees of partial melting of a fertile lherzolite protolith. There is a positive correlation between Be and Yb (Fig. 5). As ytterbium decreases during partial melting, but is not fluid mobile, we can deduce that the variation in the Be content of the Geisspfad serpentinite (Fig. 5) is directly related to the degree of partial melting. Lanzo and Huinan lherzolites are residues after partial melting of <6 to 12% (Bodinier, 1988) and of 0 to 15% (Xu et al., 2003), respectively. These lherzolites show a REE signature similar to the Geisspfad serpentinites (Fig. 10). The partial melting hypothesis is also confirmed by the extremely low whole rock Be contents of mid-Atlantic ridge ODP Leg 209 serpentinites (<0.008 µg/g; Vils et al., accepted), and of the Pindos harzburgites (<0.0016 µg/g; Pelletier et al., in review), which represent residues after high degrees of partial melting (Saccani and Photiades, 2004; Seyler et al., 2007).

The boron content of the Geisspfad serpentinite ranges from 1.8 to 4.0 µg/g. Rodingitization of some metabasites, the $\delta^{18}O$ and δD isotopic compositions, and the trace element concentrations measured in the serpentinite likely reflect interaction of serpentinite with seawater. Rocks were probably highly serpentinized before prograde metamorphism, and B was primarily added to the rock during hydrothermal activity (Bonatti et al., 1984; Agranier et al., 2007; Boschi et al., 2008; Pelletier et al., in review; Vils et al., accepted). Serpentinization conditions in the Geisspfad body were probably comparable to those occurring in the present-day Iberia abyssal plain (Agrinier et al., 1996) at low temperature (<200 °C), by analogy with the postulated tectonic setting, but no B whole rock data exist. However, the boron content of the Geisspfad serpentinite is lower than comparable low temperature mid-ocean ridge serpentinites (T<250 °C, 10.4–90.6 µg/g; Boschi et al., 2008; Vils et al., submitted). Boron has a high fluid/rock partition coefficient (~60; Scambelluri et al., 2004) during partial dehydration at high pressure (reaction: antigorite + brucite = forsterite + fluid). Geisspfad serpentinites were probably subjected to prograde dehydration reactions, suggesting that some B was lost during prograde metamorphism (Fig. 6). This boron loss was coupled to Cl loss, since Cl whole rock contents of the Geisspfad serpentinites are low (9–44 µg/g) compared to oceanic serpentinites (~100–200 µg/g; Barnes et al., 2006) and close to the primitive mantle value of 15 µg/g (Lyubetskaya and Korenaga, 2007). Coupled B and Cl loss during prograde metamorphism was also shown by Scambelluri et al. (2004).

7.4. Trace element behaviour related to the interaction with crust-derived fluids

There is a continuous increase in the Pb whole rock contents towards the ophicarbonate–metabasite contact (Fig. 5). Seitz and Hart (1973) showed that Pb may be enriched during hydrothermal alteration on the ocean floor in ultramafic systems. Li and Lee (2006) also mentioned high Pb contents (0.03–5.20 µg/g) in serpentinites from the Feather River ophiolite (California). However, the negative correlation between the Pb whole rock content and the ∂D values of the Geisspfad ultramafic rocks is better explained by interaction of these rocks with a (externally derived) crustal fluid during emplacement into the crust.

Since it is difficult to determine if the trace element compositions of the ophicarbonate and the serpentinite were similar or different prior to alpine metamorphism, the following discussion will focus on the serpentinite. In the centre of the massif, Li, Be, B, U, and Sr whole rock contents are rather constant (Fig. 5). The lithium, beryllium, and boron distribution between forsterite, antigorite, tremolite and diopside is also ± constant (Fig. 9). Serpentinite from the centre seems to have interacted with a seawater-related fluid (Fig. 7; Wenner and Taylor, 1974; Früh-Green et al., 1996), as shown by their δD and $\delta^{18}O$ values. Considering these observations, metamorphism in the centre of the massif approached closed system behavior, and Li, Be, and B contents of the minerals record equilibrium.

On the contrary, towards the rim of the massif in the serpentinite, the changes in mineral modes (Table 1) are accompanied by different trace element systematics in minerals and whole rocks, which probably reflect disequilibrium: (i) An increase of the fluid mobile element Pb in whole rocks (Fig. 5); (ii) A change in the mineral–mineral distribution of Li, Be, and B compared to the centre of the massif (Fig. 9); (iii) A shift in the Li, Be, and B contents of some rock-forming minerals (Fig. 8). The following paragraph will discuss the processes, which could generate the observed disequilibrium.

In tremolite, antigorite and diopside, Li increases from the centre of the massif to approximately 100–150 m from the contact (Figs. 8 and 9), while Li whole rock contents remain constant. The variation in the mineral Li content could be related to a redistribution of Li between the coexisting phases due to changes in mineral modes (Table 1). Because the forsterite mode is high (>40%) and constant, and forsterite has high Li contents (>2.8 µg/g, Table 4), this mineral dominates the Li budget of the whole rocks in the serpentinite (Fig. 5). The strong increase of Li in diopside, tremolite and antigorite is probably related to the low modal tremolite observed in the serpentinite at the rim of the massif (Table 1).

In the serpentinite, the B content of whole rocks and minerals remains approximately constant (Figs. 5, 8, 9). We thus propose that changes in mineral modes do not significantly affect the B content of the various minerals. In the ophicarbonate, the B content of the bulk (Fig. 5) and of antigorite increases, and to a lesser extent the B content of diopside (Fig. 8) along the northern contact. Along the southern

contact in the same rocks, no B increase is observed (Fig. 5), except in diopside and antigorite (Fig. 8). This boron increase in diopside and antigorite is most probably related to the decrease of modal tremolite towards the contact (Table 1). The difference in the B content of the ophicarbonate between the north and the south is correlated to the B content in the surrounding gneiss (Fig. 5; north: 8.79 μg/g; south: 0.92 μg/g). The gneiss showing the highest B concentration (G32a, North; Fig. 2) contains biotite, muscovite and chlorite, while the gneiss in the south (G36; Fig. 2) contains chlorite only. Muscovite and biotite are important carriers of B, in medium- to low-grade metamorphic rocks (Grew, 1996). If the fluid responsible for the observed Pb enrichment and the shift in the ∂D values of the bulk rocks is derived from the country rocks, the difference in the B content of the ultramafic rocks might be controlled by the fertility of the surrounding gneisses.

In conclusion, crustally derived fluids most probably led to B enrichment in whole rocks, as observed in some ophicarbonate, and to Pb enrichment in whole rocks, as observed in serpentinites and ophicarbonates. Apparent Li, Be, and B enrichment of some rock-forming minerals is controlled by inter-mineral redistribution, and not by a net increase of whole rock contents. There is no measurable increase of Li, B and U in most of the ultramafic massif.

7.5. Origin of the fluid

As shown by the enrichment in Pb and the low δD values in the ophicarbonate, the fluid is probably derived from the continental crust (Fig. 11). The positive correlation between the B content of the ophicarbonate and the B content in the neighboring gneiss, suggests a local origin of the fluid. The fluid propagated through the contact and probably reacted with the metabasite before infiltrating the ultramafic rocks.

Part of the original U and Pb present in the fluid probably resided in the metabasite, because epidote group minerals (zoisite, allanite) usually contain major quantities of these elements (Zack et al., 2002). For the fluid mobile elements Sr, Ce, Yb and Li no increase is observed in the serpentinite (Fig. 5). Rare earth elements (including Ce and Yb) are strongly compatible in allanite (Banks et al., 1994; Frei et al., 2004). Strontium has a similar charge and ionic radius than Eu, and should therefore be compatible in this mineral. We propose that, during fluid circulation, the metabasites acted as a filter for some elements, most notably Sr, Ce, and Yb, that were accommodated by epidote. Part of the original (crustal) Li could have been incorporated in chlorite (Li: 27.6–75.2 μg/g, Table 4), because the mineral/fluid partition coefficient of the latter is relatively high ($^{Li}D_{chlorite/fluid}$ = 0.256; Marschall et al., 2007) compared to partition coefficients published for the other minerals usually present in metabasites (Marschall et al., 2007).

We infer that the fluid flow could be triggered by dehydration of the surrounding Monte Leone gneiss. Dehydration could have occurred during prograde metamorphism or, alternatively, been active during decompression and concomitant hydration of the ultramafic rocks. We propose that interaction with crustal fluids significantly affected the trace element systematics along the border of the ultramafic rocks (Fig. 11). Fluid production during unloading of metamorphic crustal rocks at elevated temperature was observed in the Adula nappe (Central Alps) by Heinrich (1982) and postulated by Miller et al. (2002) in order to explain exhumation of high pressure metamorphic belts. Fluid migration into the core of the ultramafic rocks was perhaps limited by the massive nature of the forsterite–tremolite–antigorite fels.

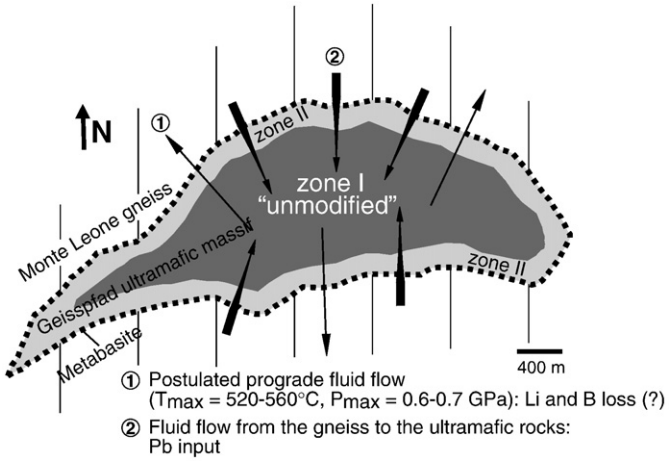

Fig. 11. Schematic representation of the different fluid migration events which occurred in the Geisspfad region between the ultramafic massif and the Monte Leone gneiss. The Geisspfad ultramafic massif is subdivided into two zones. Zone I (dark grey): the "unmodified" zone represents the rocks which conserved their prograde geochemical signature for all elements during exhumation and emplacement into the continental crust, except for the Pb enrichment in whole rocks. Zone II (light grey): this zone is characterized by an increase of Li, Be and B in some minerals due to changes in mineral modes, in addition to the Pb enrichment in whole rocks.

7.6. Implications for Li, Be and B studies of ultramafic rocks in orogenic environments

Considering the Pb content of the whole rocks, we conclude that fluid flow affected the ultramafic rocks on a distance exceeding 400 m (Figs. 5 and 12). However, the effect on the Li, Be, and B contents of minerals related to changes in mineral modes, seems to be limited to the immediate vicinity of the contact (~100–150 m, Figs. 5 and 8). For these reasons, Li, Be, and B studies in ultramafic rocks from orogenic environments, such as ultrahigh pressure terrains, which aim at detecting subduction-related signatures, should always consider and quantify the chemical and mineralogical modifications related to the emplacement into the continental crust. Such studies should include calculation of mineral modes, and trace element quantification in minerals and whole rock samples. Our study demonstrates that pronounced Li, Be and B enrichment in minerals alone does not necessarily indicate a subduction-related signature. Lead content and ∂D value of whole rock samples seem to be reliable tracers of the interaction between ultramafic rocks and crust-derived fluids.

Many ultramafic bodies embedded in continental crustal rocks are much smaller than 200 m. Studies devoted to detect subduction-related signatures in such bodies might be compromised by (late) emplacement-related fluid flow. For larger ultramafic bodies, such as the Alpe Arami garnet peridotites (1000 × 500 m) (Paquin and Altherr, 2002; Paquin et al., 2004), light element enrichment of a few μg/g in minerals should be interpreted with care. Our study demonstrated that mineral–mineral Li, Be or B redistribution can occur on a large distance due to changes in mineral modes and generate apparent enrichments.

8. Summary and conclusion

The Geisspfad massif shows mineralogical and geochemical evidence that altered oceanic ultramafic rocks might interact with the surrounding continental crust during their emplacement. In the Geisspfad ultramafic rocks, fluid–rock interaction, induced by fluids released from the surrounding gneiss, is recorded along the rim of the massif. Along a ~400 m wide border zone of the ultramafic massif, the deformation increases, the Pb whole rock content increases, and the δD is shifted to lower values towards the contact. In the serpentinite and at a maximum distance of ~150 m from the metabasite–ophicarbonate contact, the Li, Be and B concentrations of minerals are modified due to changes in mineral modes, leading to apparent enrichments. The lead enrichment observed in the serpentinite, compared to the nearly constant concentrations of some other fluid mobile elements such as Li, B or U, could be explained by the interaction of the fluid with

metabasite before infiltrating the serpentinite. In order to avoid equivocal interpretations of Li, Be, and B distributions of orogenic ultramafic rocks, light element studies should focus on rather large ultramafic bodies of several hundreds of meters wide.

Acknowledgements

We thank E. Gnos, A. Berger, T. Ludwig and H.-P. Meyer for analytical support, T. Plank (Boston University) for the ICP-MS analyses, and B. Putlitz for her help during stable isotopic analyses. We are grateful to V. Serneels for whole rock analyses carried out at the University of Fribourg. This work was financially supported by grants of the Swiss NSF (200020-112149) to A. Kalt. We acknowledge financial support by the Swiss NSF grant 200021-103479/1 and by the Canton of Bern for the electron microprobe facility at the Institute of Geological Sciences, University of Bern. We also thank the Hungarian financial support to the Institute of Isotopes of the Hungarian Academy of Sciences in Budapest, GVOP-3.2.1-2004-04-0268/3.0 and NAP VENEUS05 Contract No. OMFB 00184/2006.

References

Agrinier, P., Cornen, G., Beslier, M.-O., 1996. Mineralogical and oxygen isotopic features of serpentinites recovered from the ocean/continent transition in the Iberia Abyssal Plain. In: Whitmarsh, R.B., Sawyer, D.S., Klaus, A., Masson, D.G. (Eds.), Proceedings of the Ocean Drilling Program Scientific Results, vol. 149, pp. 541–552.

Agranier, A., Lee, C.-T.A., Li, Z.-X.A., Leeman, W.P., 2007. Fluid Mobile Element Budgets in Serpentinized Oceanic Lithospheric Mantle: Insights from B, As, Li, Pb, PGEs and Os Isotopes in the Feather River ophiolite, California. Chemical Geology. doi:10.1016/j.chemgeo.2007.08.008.

Allan, J.F., Dick, H.J.B., 1996. Cr-rich spinel as a tracer for melt migration and melt-wall rock interaction in the mantle: Hess Deep, leg 147. Proceedings of the Ocean Drilling Program Scientific Results 147, 157–172.

Anderson, D.L., Kasztovszky, Z., 2004. Application of PGAA with neutron beam. In: Molnár, G.L. (Ed.), Handbook of Prompt Gamma Activation Analysis with Neutron Beams. Springer, Kluwer Academic Publisher, Amsterdam, pp. 148–152.

Arai, S., 1994. Characterization of spinel peridotites by olivine-spinel compositional relationships: review and interpretation. Chemical Geology 113, 191–204.

Banks, D.A., Yardley, B.W.D., Campell, A.R., Jarvis, K.E., 1994. REE composition of an aqueous magmatic fluid: a fluid inclusion study from the Capitan Pluton, New Mexico, USA. Chemical Geology 110, 299–314.

Barnes, J.D., Selverstone, J., Sharp, Z.D., 2006. Chlorine isotope chemistry of serpentinites from Elba, Italy, as an indicator of fluid source and subsequent tectonic history. Geochemistry, Geophysics and Geosystems 7 (8). doi:10.1029/2006GC001296.

Benton, L.D., Ryan, J.G., Tera, F., 2001. Boron isotope systematics of slab fluids as inferred from a serpentine seamount, Mariana forearc. Earth and Planetary Science Letters 187, 273–282.

Benton, L.D., Ryan, J.G., Savov, I.P., 2004. Lithium abundance and isotope systematics of forearc serpentinites, Conical Seamount, Mariana forearc: insights into the mechanics of slab-mantle exchange during subduction. Geochemistry, Geophysics and Geosystems 5 (8). doi:10.1029/2004GC000708.

Bodinier, J.L., 1988. Geochemistry and petrogenesis of the Lanzo peridotite body, western Alps. Tectonophysics 149, 67–88.

Bodinier, J.-L., Godard, M., 2004. Orogenic, ophiolitic, and abyssal peridotites. In: Carlson, R.W., Holland, H.D., Turekian, K.K. (Eds.), Treatise on Geochemistry Volume 2: The Mantle and Core. Elsevier, Oxford, pp. 103–170.

Boillot, G., Grimaud, S., Mauffret, A., Mougenot, D., Kornprobst, J., Mergoildaniel, J., Torrent, G., 1980. Ocean-continent boundary off the Iberian margin—a serpentinite diapir west of the Galicia Bank. Earth and Planetary Science Letters 48, 23–34.

Bonatti, E., Lawrence, J.R., Morandi, N., 1984. Serpentinization of oceanic peridotites: temperature dependence of mineralogy and boron content. Earth and Planetary Science Letters 70, 88–94.

Boschi, C., Dini, A., Früh-Green, G.L., Kelley, D.S., 2008. Isotopic and element exchange during serpentinization and metasomatism at the Atlantis Massif (MAR 30°N): insights from B and Sr isotope data. Geochimica et Cosmochimica Acta 72, 1801–1823.

Brenan, J.M., Neroda, E., Lundstrom, C.C., Shaw, H.F., Ryerson, F.J., Phinney, D.L., 1998a. Behaviour of boron, beryllium, and lithium during melting and crystallization: constraints from mineral-melt partitioning experiments. Geochimica et Cosmochimica Acta 62 (12), 2129–2141.

Brenan, J.M., Ryerson, F.J., Shaw, H.F., 1998b. The role of aqueous fluids in the slab-to-mantle transfer of boron, beryllium, and lithium during subduction: experiments and models. Geochimica et Cosmochimica Acta 62 (19–20), 3337–3347.

Chan, L.-H., Edmond, J.M., Thompson, G., Gillis, K., 1992. Lithium isotopic composition of submarine basalts: implications for the lithium cycle in the oceans. Earth and Planetary Science Letters 108, 151–160.

Currie, L.A., 1968. Limits for qualitative detection and quantitative determination. Analytical Chemistry 40, 586–593.

Decitre, S., Deloule, E., Reisberg, L., James, R., Agrinier, P., Mével, C., 2002. Behavior of Li and its isotopes during serpentinization of oceanic peridotites. Geochemistry, Geophysics and Geosystems 3 (1). doi:10.1029/2001GC000178.

Evans, B.W., Trommsdorff, V., 1970. Regional metamorphism of ultramafic rocks in the Central Alps: parageneses in the system CaO–MgO–SiO_2–H2O. Schweizerische Mineralogische und Petrographische Mitteillungen 50, 481–492.

Frei, D., Liebscher, A., Franz, G., Dulski, P., 2004. Trace element geochemistry of epidote minerals. Reviews in Mineralogy & Geochemistry 56, 553–605.

Früh-Green, G.L., Weissert, H., Bernoulli, D., 1990. A multiple fluid history recorded in alpine ophiolites. Journal of the Geological Society 147, 959–970.

Früh-Green, G.L., Plas, A., Lécuyer, C., 1996. Petrologic and stable isotope constraints on hydrothermal alteration and serpentinization of the EPR shallow mantle at Hess Deep (site 895). Proceedings of the Ocean Drilling Program Scientific Results 147, 255–288.

Gao, S., Luo, T., Zhang, B., Zhang, H., Han, Y., Zhao, Z., Hu, Y., 1998. Chemical composition of the continental crust as revealed by studies in East China. Geochimica et Cosmochimica Acta 62, 1959–1975.

Gméling, K., Harangi, S., Kasztovszky, Z., 2005. Boron and chlorine concentration of volcanic rocks: an application of prompt gamma activation analysis. Journal of Radioanalytical and Nuclear Chemistry 265, 201–212.

Govindaraju, K., 1994. Compilation of working values and sample description for 383 geostandards. Geostandards Newsletter 18, 1–158.

Grew, E.S., 1996. Borosilicates (exclusive of tourmaline) and Boron in rock-forming minerals in metamorphic environments. Reviews in Mineralogy 33, 387–502.

Heinrich, C.A., 1982. Kyanite–eclogite to amphibolite facies evolution of hydrous mafic and pelitic rocks, Adula nappe, Central Alps. Contributions to Mineralogy and Petrology 81, 30–38.

Kasemann, S., Meixner, A., Rocholl, A., Vennemann, T., Schmitt, A., Wiedenbeck, M., 2001. Boron and oxygen isotope composition of certified reference materials NIST SRM 610/612, and reference materials JB-2G and JR-2G. Geostandards Newsletter 25, 405–416.

Kelley, K.A., Plank, T., Ludden, J., Staudigel, H., 2003. Composition of altered oceanic crust at ODP Sites 801 and 1149. Geochemistry Geophysics Geosystems 4. doi:10.1029/2002GC000435.

Keusen, H.-R., 1970. Genese der basischen und ultrabasischen Gesteine vom Geisspfad (Wallis, Schweiz). Vortragsreferat DMG. Fortschritte der Mineralogie 48 (1), 14–16.

Keusen, H.-R., 1972. Mineralogie und Petrographie des metamorphen Ultramafitit-Complexes vom Geisspfad (Penninische Alpen). Schweizerische Mineralogische und Petrographische Mitteillungen 52 (3), 385–478.

Leeman, W.P., 1996. Boron and other fluid-mobile elements in volcanic arc lavas: implications for subduction processes. In: Bebout, G.E., Scholl, D., Kirby, S., Platt, J.P. (Eds.), Subduction Top to Bottom, AGU Geophysical Monograph Series, vol. 96, pp. 269–276.

Li, Z.-X.A., Lee, C.-T.A., 2006. Geochemical investigation of serpentinized oceanic lithospheric mantle in the Feather River Ophiolite, California: implications for the recycling rate of water by subduction. Chemical Geology 235, 161–185.

Lyubetskaya, T., Korenaga, J., 2007. Chemical composition of Earth's primitive mantle and its variance: 1. Method and results. Journal of Geophysical Research 112, 1–21.

Manatschal, G., Nievergelt, P., 1997. A continent–ocean transition recorded in the Err and Platta nappes (Eastern Switzerland). Eclogae geolocea Helveticea 90, 3–27.

Manatschal, G., Müntener, O., Desmurs, L., Bernoulli, D., 2003. An ancient ocean–continent transition in the Alps: the Totalp, Err-Platta, and Malenco units in the eastern Central Alps (Graubünden and northern Italy). Eclogae geolocea Helveticea 96, 131–146.

Marroni, M., Molli, G., Montanini, A., Tribuzio, R., 1998. The association of continental crust rocks with ophiolites in the Northern Apennines (Italy): implications for the continent–ocean transition in the Western Tethys. Tectonophysics 292, 43–66.

Marschall, H.R., 2005. Lithium, beryllium and boron in high-pressure metamorphic rocks from Syros (Greece). Mathematisch-Naturwissenschaftlichen Gesamtfakultät, Ruprecht-Karls-Universität, Heidelberg (Germany), p. 411.

Marschall, H.R., Ludwig, T., 2004. The low-boron contest: minimising surface contamination and analysing boron concentrations at the ng/g-level by secondary ion mass spectrometry. Mineralogy and Petrology 81, 265–278.

Marschall, H.R., Kasztovszky, Z., Gméling, K., Altherr, R., 2005. Chemical analysis of high-pressure metamorphic rocks by PGNAA: comparison with results from XRF and solution ICP-MS. Journal of Radioanalytical and Nuclear Chemistry 265, 339–348.

Marschall, H.R., Altherr, R., Rüpke, L., 2007. Squeezing out the slab—modelling the release of Li, Be and B during progressive high-pressure metamorphism. Chemical Geology 239, 323–335.

McDonough, W.F., Sun, S.-S., 1995. The composition of the Earth. Chemical Geology 120, 223–253.

Miller, J.A., Buick, I.S., Cartwright, I., Barnicoat, A., 2002. Fluid processes during the exhumation of high-P metamorphic belts. Mineralogical Magazine 66 (1), 93–119.

Molnár, G.L., 2004. Handbook of prompt gamma activation analysis with neutron beams. Springer, Amsterdam.

Müntener, O., Hermann, J., Trommsdorff, V., 2000. Cooling history and exhumation of lower-crustal granulite and upper mantle (Malenco, Eastern Central Alps). Journal of Petrology 41, 175–200.

Müntener, O., Piccardo, G.B., Polino, R., Zanetti, A., 2005. Revisiting the Lanzo peridotite (NW-Italy): "Asthenospherization" of ancient mantle lithosphere. Ofioliti 30 (2), 111–124.

Niu, Y., 2004. Bulk-rock major and trace element compositions of abyssal peridotites: Implications for mantle melting, melt extraction and post-melting processes beneath mid-ocean ridges. Journal of Petrology 45 (12), 2423–2458.

Noll, J.P.D., Newsom, H.E., Leeman, W.P., Ryan, J.G., 1996. The role of hydrothermal fluids in the production of subduction zone magmas: evidence from siderophile and chalcophile trace elements and boron. Geochimica et Cosmochimica Acta 60, 587–611.

Ottolini, L., Bottazzi, P., Vannucci, R., 1993. Quantification of lithium, beryllium, and boron in silicates by secondary ion mass spectrometry using conventional energy filtering. Analytical Chemistry 65 (15), 1960–1968.

Ottolini, L., Le Fèvre, B., Vannucci, R., 2004. Direct assessment of mantle boron and lithium contents and distribution by SIMS analyses of peridotite minerals. Earth and Planetary Science Letters 228, 19–36.

Palmer, M.R., 1991. Boron isotope systematics of hydrothermal fluids and tourmalines: a synthesis. Chemical Geology (Isotope Geoscience Section) 94, 111–121.

Palmer, M.R., 1996. Hydration and uplift of the oceanic crust on the Mid-Atlantic Ridge associated with hydrothermal activity: evidence from boron isotopes. Geophysical Research Letters 23, 3479–3482.

Paquin, J., Altherr, R., 2002. Subduction-related lithium metasomatism during exhumation of the Alpe Arami ultrahigh-pressure garnet peridotite (Central Alps, Switzerland). Contributions to Mineralogy and Petrology 143, 623–640.

Paquin, J., Altherr, R., Ludwig, T., 2004. Li–Be–B systematics in the ultrahigh-pressure garnet peridotite from Alpe Arami (Central Swiss Alps): implications for slab-to-mantle wedge transfer. Earth and Planetary Science Letters 218, 507–519.

Pastorelli, S., 1994. Il complesso ultrafemico di Geisspfad e i suori rapporti con le rocce incassanti. unpublished diploma thesis, Facolta di scienze M.F.N. Universita degli studi di Torino, Torino, 119 p.

Pastorelli, S., Martinotti, G., Piccardo, G.B., Rampone, E., Scambelluri, M., 1995. The Geisspfad Complex and its relationships with the Monte Leone Nappe (Lower Pennine, Western Alps). In: Polino, R., Sacchi, R. (Eds.), Atti del Convegno Rapporti Alpi-Appennino 1994. Accad. Naz. Scienze, Scritti e Documenti 14, Roma, pp. 349–358.

Paulick, H., Bach, W., Godard, M., De Hoog, J.C.M., Suhr, G., Harvey, J., 2006. Geochemistry of abyssal peridotites (Mid-Atlantic Ridge, 15°′N, ODP Leg 209): implications for fluid/rock interaction in slow spreading environments. Chemical Geology 234, 179–210.

Pelletier, L., Vils, V., Kalt, A., Gméling, K., Li, B., in review. Be contents of harzburgites from the Dramala Complex (Pindos ophiolite, Greece): a MOR-type mantle in a supra-subduction zone environment. Journal of Petrology.

Plyusnina, L.P., 1982. Geothermometry and geobarometry of plagioclase-hornblende bearing assemblages. Contributions to Mineralogy and Petrology 80 (2), 140–146.

Preiswerk, H., 1901. Über Dunitserpentin am Geisspfadpass im Oberwallis. Dissertation University of Basel (Switzerland), Birkhäuser.

Révay, Z., Belgya, T., 2004. Principles of PGAA method. In: Molnár, G.L. (Ed.), Handbook of Prompt Gamma Activation Analysis with Neutron Beams. Springer, Kluwer Academic Publisher, Amsterdam, pp. 1–30.

Révay, Z., Belgya, T., Kasztovszky, Z., Weil, J.L., Molnár, G.L., 2004. Cold neutron PGAA facility at Budapest. Nuclear Instruments and Methods in Physics Research Section B: Beam Interactions with Materials and Atoms 213, 385–388.

Rosner, M., Erzinger, J., Franz, G., Trumbull, R.B., 2003. Slab-derived boron isotope signatures in arc volcanic rocks from the Central Andes and evidence for boron isotope fractionation during progressive slab dehydration. Geochemistry, Geophysics and Geosystems 4. doi:10.1029/2002GC000438.

Rudnick, R.L., Fountain, D.M., 1995. Nature and composition of the continental crust; a lower crustal perspective. Reviews in Geophysics 33, 267–309.

Rudnick, R.L., Gao, S., 2004. Composition of the continental crust. In: Holland, H.D., Turekian, K.K. (Eds.), Treatise on Geochemistry, vol. 3, pp. 1–64.

Rumble, D., Hoering, T.C., 1994. Analysis of oxygen and sulfur isotope ratios in oxide and sulfide minerals by spot heating with a carbon dioxide laser in a fluorine atmosphere. Accounts of Chemical Research 27, 237–241.

Saccani, E., Photiades, A., 2004. Mid-ocean ridge and supra-subduction affinities in the Pindos ophiolites (Greece): implications for magma genesis in forearc setting. Lithos 73, 229–253.

Sanford, R.F., 1982. Growth of ultramafic reaction zones in greenschist to amphibolite facies metamorphism. American Journal of Science 282, 543–616.

Savov, I.P., Ryan, J.G., D'Antonio, M., Kelly, K., Mattie, P., 2005. Geochemistry of serpentinized peridotites from the Mariana Forearc Conical Seamount, ODP Leg 125: Implications for the elemental recycling at subduction zones. Geochemistry Geophysics Geosystems 6 (4). doi:10.1029/2004GC000777.

Savov, I.P., Ryan, J.G., D'Antonio, M., Fryer, P., 2007. Shallow slab fluid release across and along the Mariana arc-basin system: Insights from geochemistry of serpentinized peridotites from the Mariana fore arc. Journal of Geophysical Research 112. doi:10.1029/2006JB004479.

Scambelluri, M., Müntener, O., Ottolini, L., Pettke, T., Vannucci, R., 2004. The fate of B, Cl and Li in the subducted oceanic mantle and in the antigorite breakdown fluids. Earth and Planetary Science Letters 222, 217–234.

Scambelluri, M., Hermann, J., Morten, L., Rampone, E., 2006. Melt-versus fluid-induced metasomatism in spinel to garnet wedge peridotites (Ulten Zone, Eastern Italian Alps): clues from trace element and Li abundances. Contributions to Mineralogy and Petrology 151, 372–394.

Schmid, S.M., Fügenschuh, B., Kissling, E., Schuster, R., 2004. Tectonic map and overall architecture of the Alpine orogen. Eclogae Geologicea Helveticea 97 (1), 93–117.

Schmidt, K., Koschinsky, A., Garbe-Schönberg, D., De Carvalho, L.M., Seifert, R., 2007. Geochemistry of hydrothermal fluids from the ultramafic-hosted Logatchev hydrothermal field, 15°N on the Mid-Atlantic Ridge: temporal and spatial investigation. Chemical Geology 242, 1–21.

Seitz, M.G., Hart, S.R., 1973. Uranium and boron distributions in some oceanic ultramafic rocks. Earth and Planetary Science Letters 21, 97–107.

Seyfried, W.E., Janecky, D.R., Mottl, M.J., 1984. Alteration of the oceanic crust: implications for geochemical cycles of lithium and boron. Geochimica et Cosmochimica Acta 48, 557–569.

Seyler, M., Lorand, J.P., Dick, H.J.B., Drouin, M., 2007. Pervasive melt percolation reactions in ultra-depleted refractory harzburgites at the Mid-Atlantic Ridge, 15° 20′N: ODP Hole 1274A. Contributions to Mineralogy and Petrology 153, 303–319.

Sharp, Z.D., 1990. A laser-based microanalytical method for the in-situ determination of oxygen isotope ratios of silicates and oxides. Geochimica et Cosmochimica Acta 54, 1353–1357.

Sharp, Z.D., Atudorei, V., Durakiewicz, T., 2001. A rapid method for determination of hydrogen and oxygen isotope ratios from water and hydrous minerals. Chemical Geology 178 (1–4), 197–210.

Spivack, A.J., Edmond, J.M., 1987. Boron isotope exchange between seawater and the oceanic crust. Geochimica et Cosmochimica Acta 51 (5), 1033–1043.

Szakmány, G., Kasztovszky, Zs., 2004. Prompt Gamma Activation Analysis, a new method in the archaeological study of polished stone tools and their raw materials. European Journal of Mineralogy 16 (2), 285–295.

Taylor, S.R., McLennan, S.M., 1995. The geochemical evolution of the continental crust. Reviews in Geophysics 33, 241–265.

Teng, F.-Z., McDonough, W.F., Rudnick, R.L., Walker, R.J., 2006. Diffusion-driven extreme lithium isotopic fractionation in country rocks of the Tin Mountain pegmatite. Earth and Planetary Science Letters 243 (3–4), 701–710.

Thompson, G., Melson, W.G., 1970. Boron contents of serpentinites and metabasalts in the oceanic crust: implications for the boron cycle in the oceans. Earth and Planetary Science Letters 8, 61–65.

Tomascak, P.B., 2004. Developments in the understanding and application of lithium isotopes in the Earth and Planetary sciences. Reviews in Mineralogy and Geochemistry 55, 153–195.

Vils, F., Pelletier, L., Kalt, A., Müntener, O., Ludwig, T. The lithium, boron and beryllium content of serpentinized peridotites from ODP leg 209 (sites 1272A and 1274A): implications for lithium and boron budgets of oceanic lithosphere. Geochimica et Cosmochimica Acta, accepted pending revisions.

Wedepohl, K.H., 1995. The composition of the continental crust. Geochimica et Cosmochimica Acta 59, 1217–1232.

Wei, W., Kastner, M., Deyhle, A., Spivack, A.J., 2005. Geochemical cycling of fluorine, chlorine, bromine, and boron and implications for fluid-rock reactions in Mariana forearc, South Chamorro Seamount, ODP Leg 195. Proceedings of the Ocean Drilling Program, Scientific Results 195, 1–23.

Wenner, D.B., Taylor Jr., H.P., 1974. D/H and 18O/16O studies of serpentinization of ultramafic rocks. Geochimica et Cosmochimica Acta 38, 1255–1286.

Xu, Y.-G., Menzies, M.A., Thirlwall, M.F., Huang, X.-L., Liu, Y., Chen, X.-M., 2003. "Reactive" harzburgites from Huinan, NE China: Products of the lithosphere–asthenosphere interaction during lithospheric thinning? Geochimica et Cosmochimica Acta 67 (3), 487–505.

You, C.-F., Spivack, A.J., Gieskes, J.M., Rosenbauer, R., Bischoff, J.L., 1995. Experimental study of boron geochemistry: implications for fluid processes in subduction zones. Geochimica et Cosmochimica Acta 59, 2435–2442.

Zack, T., Foley, S.F., Rivers, T., 2002. Equilibrium and disequilibrium trace element partitioning in hydrous eclogites (Trescolmen, Central Alps). Journal of Petrology 43 (10), 1947–1974.

Zierenberg, R.A., Fouquet, R.A., Miller, D.J., Bahr, J.M., Naker, P.A., Bjerkgard, T., Brunner, C.A., Duckworth, R.C., Gable, R., Gieskes, J.M., Goodfellow, W.D., Groschel-Becker, H.M., Guerin, G., Ishibashi, J., Iturrino, G., James, R.H., Lackschewitz, K.S., Marquez, L.L., Nehlig, P., Peter, J.M., Rigsby, C.A., Schultheiss, P., Shanks, W.C., Simoneit, B.R.T., Summit, M., Teagle, D.A.H., Urabt, M., Zuffa, G.G., 1998. The deep structure of a sea-floor hydrothermal deposit. Nature 392 (6675), 485–488.